Review

Corrosion Behavior of High Entropy Alloys and Their Application in the Nuclear Industry—An Overview

Tianrun Li [1,2,†], **Debin Wang** [1,2,†], **Suode Zhang** [1] **and Jianqiang Wang** [1,*]

1   Shenyang National Laboratory for Materials Science, Institute of Metal Research,
    Chinese Academy of Sciences, Shenyang 110016, China
2   School of Materials Science and Engineering, University of Science and Technology of China,
    Shenyang 110016, China
*   Correspondence: jqwang@imr.ac.cn
†   These authors contributed equally to this work.

Abstract: With multiple principal components, high entropy alloys (HEAs) have aroused great interest due to their unique microstructures and outstanding properties. Recently, the corrosion behavior of HEAs has become a scientific hotspot in the area of material science and engineering, and HEAs can exhibit good protection against corrosive environments. A comprehensive understanding of the corrosion mechanism of HEAs is important for further design of HEAs with better performance. This paper reviews the corrosion properties and mechanisms of HEAs (mainly Cantor alloy and its variants) in various environments. More crucially, this paper is focused on the influences of composition and microstructure on the evolution of the corrosion process, especially passive film stability and localized corrosion resistance. The corrosion behavior of HEAs as structural materials in nuclear industry applications is emphasized. Finally, based on this review, the possible perspectives for scientific research and engineering applications of HEAs are proposed.

Keywords: high-entropy alloy; corrosion resistance; passive film; heterogeneous structure; lead–bismuth eutectic; supercritical water

1. Introduction

High entropy alloys (HEAs) or multi-principal elements alloys (MPEAs), generally consist of five or more principal elements in equimolar ratios and possess high molar mixing entropy (>1.6 R), however, this definition is not mandatory for the discovery and development of new alloys [1]. This kind of alloys breaks the conventional design philosophy of single principal component alloys and stabilizes the solid solution rather than intermetallic compound. The appearance of HEAs broadens the window of alloy composition design and explores the medium position of the phase diagrams. HEAs exhibit four unique core effects: the high-entropy effect, the lattice distortion effect, the sluggish diffusion effect, and the cocktail effect, which provides an impressive series of mechanical properties [2,3]. Compared to conventional metallic alloys, HEAs present superior mechanical properties, such as good ductility, high toughness, and outstanding fatigue resistance. In addition, some HEAs exhibit uniform passive films [4], high temperature phase stability [5], and lattice distortion [6–8], and thus possess application potentials as corrosion resistant materials, high-temperature structural materials, and irradiation tolerant materials. Therefore, many attempts and explorations have been made to apply HEAs to these novel fields.

HEAs can exhibit good protection against corrosive environments, which is attributed to the element effect and microstructure effect. Firstly, a large number of corrosion resistant elements can be solidly dissolved in HEAs, such as Cr, Mo, Ti, and other passivation elements, which provides protection ability by forming dense and stable passive film [4,9–12]. The unique dissolution and passivation process of HEA as well as the synergistic action between multiple elements may account for their unique corrosion

properties, differing from that of traditional alloys. Secondly, owing to the high entropy effect, HEAs are inclined to form the structure of simple solid solutions [13–15]. The disordered arrangement of different atoms in these solid solutions leads to a locally random chemical environment, promoting the growth of single and continuous passive film, particularly in single-phase solid solution. Nevertheless, single-phase HEAs cannot satisfy the demands of strength and toughness matching; a lack of strength for face centered cubic (FCC) alloys and toughness for body centered cubic (BCC) alloys. The heterogeneous structure of multi-phases can enhance the compatibility of strength and toughness, but this inevitably initiates localized corrosion [16,17]. Currently, most of corrosion-related works in HEAs are focused on the elemental interactions and the design of high corrosion resistant alloys, as well as the improvement of corrosion resistance by modifying microstructure.

HEAs also show potential applications as structural materials of nuclear power [18–20]. Candidate structural materials for the Generation-IV nuclear power system (Gen-IV) must stay reliable in extreme conditions, such as liquid lead–bismuth eutectic (LBE), supercritical water (SCW), and so on. The motivation for transitioning away from zirconium-based fuel cladding to significantly more oxidation-resistant materials, thereby enhancing safety margins during severe accidents, is laid out. To design accident-tolerant fuel cladding is an urgent need. The degradation of material properties can occur inevitably due to radiation damage, high temperature phase transition, and corrosion. Among the proposed coated zirconium-based cladding are, ferritic alumina-forming alloy cladding [21], and silicon carbide [22,23]. These materials are less resistant to corrosion. Compared to the commercial alloys, the severe lattice distortion and the sluggish diffusion can provide an enhanced neutron swelling resistance and phase stability for HEAs [7,24]. Recently, more attention has been focused on the corrosion resistance of HEA in these environments.

In this review, the corrosion behaviors and mechanisms of HEAs in various environments are elucidated, as shown in Figure 1. Firstly, the electrochemical and passivation behaviors of common elements in HEAs are summarized, and their mechanisms of protection or deterioration are elaborated. These understandings are beneficial to perform the composition design of specific corrosion resistant HEAs. Secondly, microstructure-dependence on the local corrosion properties of HEAs is reviewed, which is helpful for the regulation and control of the microstructure of the HEAs with excellent corrosion resistance. Subsequently, some features and the related mechanisms of HEAs in the nuclear industry are briefly discussed, which is most likely to expand the application field of HEAs. Finally, on the basis of this overview, the possible perspectives for scientific research and engineering applications of HEAs are provided.
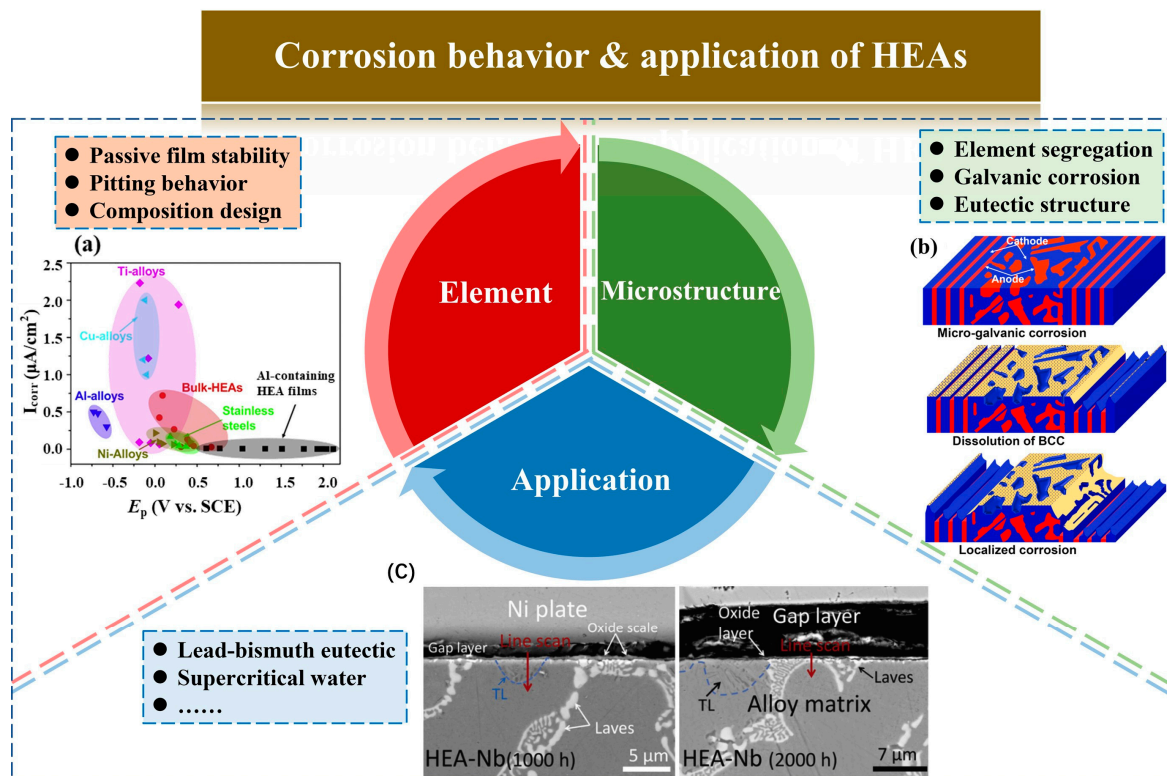
Figure 1. An overview of corrosion behavior and mechanism of HEAs regarding their elements (red area), microstructure (green area), and applications (blue area). (**a**) Passive film stability and pitting behavior for various alloys; (**b**) corrosion mechanism diagram of EHEA in H_2SO_4 solution; (**c**) SEM results of the cross section of HEAs after LBE corrosion [25–27].

2. Influence of Elements on the Corrosion of HEAs

A large selection window for element types and contents is characteristic of HEAs. The flexibility of composition design customizes many impressive properties, such as the integration of strength and toughness, oxidation resistance, as well as corrosion resistance. However, it is still not clear how the specific element contributes to the corrosion resistance in aqueous solution. Exploring the dissolution, passivation tendency, and pitting behavior of alloying elements in HEA systems is helpful for the design of corrosion resistant components.

2.1. Chromium

Chromium (Cr) is the principal element that provides corrosion resistance to most of the HEAs as well as to conventional alloys, because the passive films containing $Cr_2O_3/Cr(OH)_3$ are relatively compact and protective [4,28–31]. Chai et al. [32] reported that FeCoNi experienced active–passive corrosion behavior during the polarization process, while the active–passive process was obviously inhibited for $FeCoNiCr_{0.5}$ as seen in Figure 2a. This indicated the introduction of Cr contributed to form a stable passive film. In addition, the passive current density (i_{pass}) was significantly reduced, while the resistance of charge transfer (R_t) as well as the phase shift (n_{dl}) increased with the addition of Cr. These results showed that a more stable passive film was prone to growing on the Cr-rich alloys. Cr also contributes to the improvement of localized corrosion. It is generally acknowledged that the pitting process are determined by both pitting initiation and stable growth. As displayed in Figure 2b, when the content of Cr increased from 0 to 0.5, the pit corrosion potential (E_{pit}) elevated from 0.174 to 0.453 V_{SCE}. Meanwhile, R_t of $FeCoNiCr_{0.5}$ reached about 2×10^4 Ω cm^2, which was an order of magnitude higher than that of FeCoNi (Figure 2c–e), implying that the initiation of pitting corrosion was also retarded.
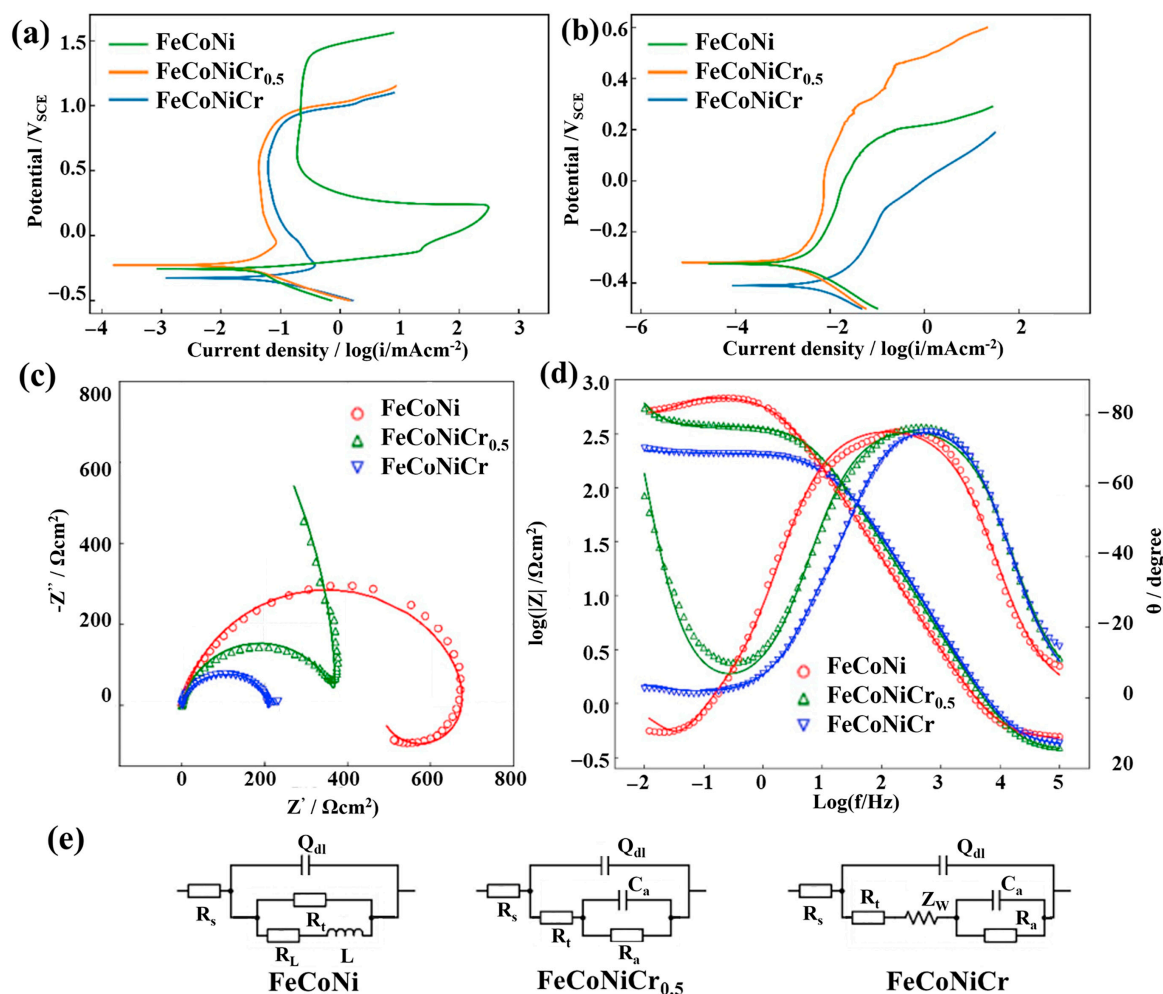
Figure 2. The polarization and EIS performance of FeCoNiCr$_x$ (x = 0, 0.5, 1) HEAs. Potentiodynamic curves for FeCoNiCr$_x$ in (**a**) H$_2$SO$_4$ aqueous solution (0.5 M) and (**b**) NaCl aqueous solution (3.5 wt.%); (**c**–**e**) the Nyquist, Bode curves and electrical equivalent circuit for FeCoNiCr$_x$ in 0.5 M H$_2$SO$_4$ aqueous solution [32].

The passivation ability of Cr is influenced by other alloy elements. Generally, it is acknowledged that the content of Cr should exceed 12 at.% to achieve perfect passivation. However, it was unexpected that the CoCrFeMnNi HEA containing 20 at.% Cr exhibited rather inferior corrosion resistance in a Cl-containing solution. From the perspective of the solubility–diffusion–deposition model, Feng et al. [33] explained the reason why Cr-containing HEA was difficult to passivate in a Cl⁻ environment. In the CoCrFeMnNi alloy system, Cr could serve as the dominating film formation element providing protection for the alloys, and other elements exhibited interactions with Cr. Ni could block the dissolution of Cr atoms due to its almost insoluble features. Fe promoted the generation of H⁺ by hydrolysis and reduced the supersaturation of oxides/hydroxides on account of the rather high solubility product. Mn and Co were difficult to deposit their oxides/hydroxides upon the surface due to the high content of H⁺ produced by the hydrolysis reaction. These factors restrained the formation of protective oxide and hydroxide. Therefore, CoCrFeMnNi exhibited rather weak passivation ability despite the high content of Cr.

2.2. Titanium

Generally, titanium (Ti) performs well in passivation for pure Ti and conventional alloys, because the protective TiO$_2$-based passive film can spontaneously develop upon the surface. Therefore, the addition of Ti into HEAs exhibits an excellent passive ability due to

the formation of a TiO$_2$-rich film. It exhibited spontaneous passivation for AlCoCrFeNiTi$_x$ (without going through the active state) at high Ti content, while active–passive transition occurred without the addition of Ti, as shown in Figure 3a [34]. Simultaneously, i_{pass} significantly decreased as the Ti content increased from 0 to 0.6 at.%, which indicated that Ti facilitated the formation and stability of passive film. Furthermore, it was noted that the E_{pit} of Al$_{2-x}$CoCrFeNiTi$_x$ increased with the addition of Ti (Figure 3b) [9]. Meanwhile, Figure 3c–e shows that the number and size of pits decreased, demonstrating that Ti was beneficial for pitting resistance. This was due to the appearance of an unoxidized metal state as indicated in the X-ray photoelectron spectroscopy (XPS) results (Figure 3f,g), which inhibited the transport of point defects.
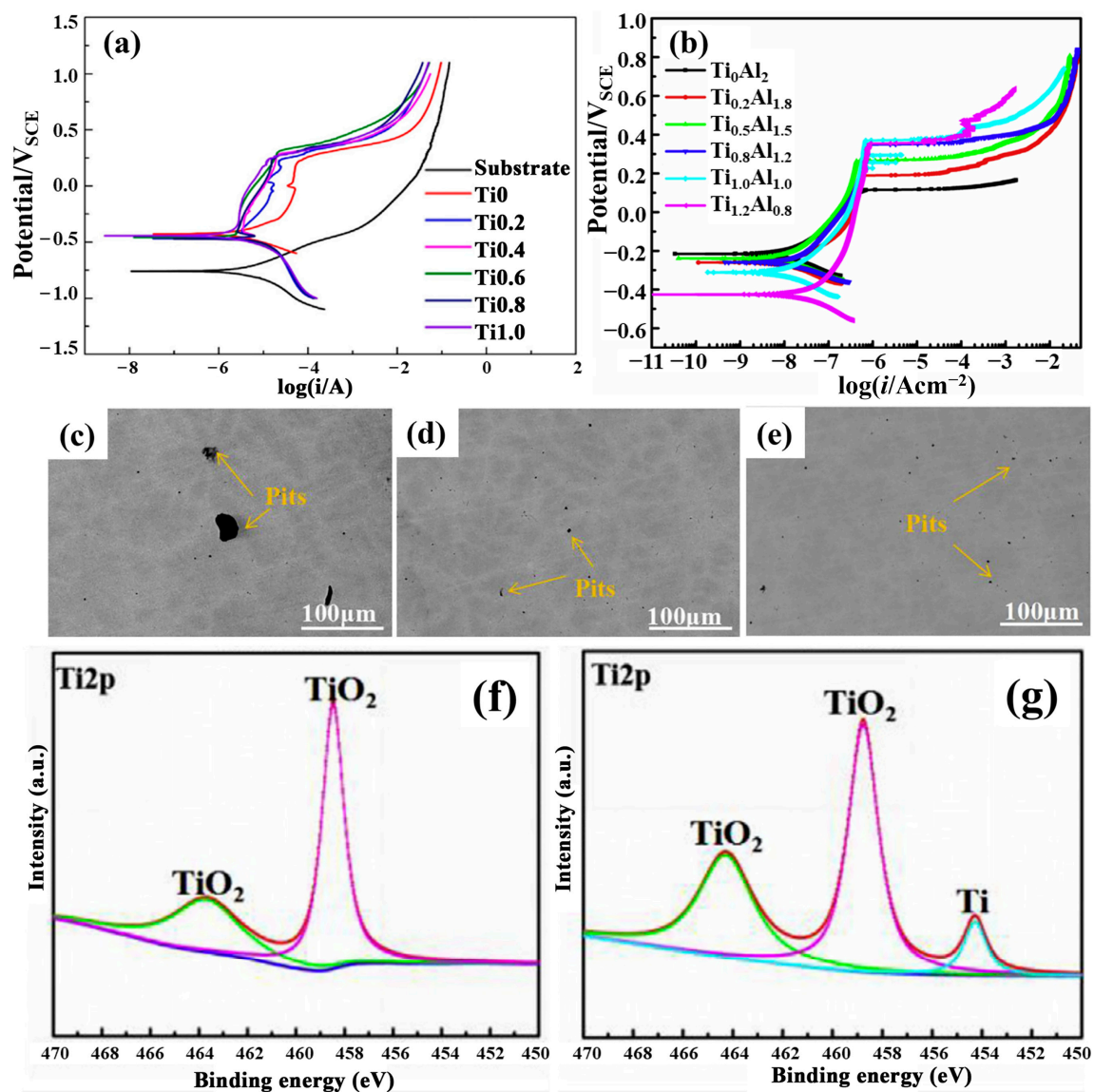

Figure 3. The electrochemical polarization performance, corrosion morphologies, and XPS results for Ti-containing HEAs. (**a**) Potentiodynamic polarization curves of AlCoCrFeNiTi$_x$ (x = 0, 0.2, 0.4, 0.6, 0.8, and 1.0) coatings and AISI1045 steel substrate; (**b**) potentiodynamic polarization plots of Al$_{2-x}$CoCrFeNiTi$_x$; corrosion morphologies of Al$_{2-x}$CoCrFeNiTi$_x$ HEAs after the potentiodynamic polarization in 3.5 wt.% NaCl aqueous solution: (**c**) Ti$_0$Al$_2$, (**d**) Ti$_{0.2}$Al$_{1.8}$, (**e**) Ti$_{0.5}$Al$_{1.5}$; XPS results of the surface films upon (**f**) Ti$_{0.5}$Al$_{1.5}$, and (**g**) Ti$_{1.0}$Al$_{1.0}$ HEAs [9,34].

2.3. Molybdenum

Molybdenum (Mo) serves as a crucial pitting resistant element for traditional stainless-steel materials in chloride-containing environment. Different to Cr, the passive film cannot form completely on pure Mo and the Mo-containing oxides grow due to the chemisorption of a monolayer of oxygen [35,36]. The Mo-containing oxides are incorporated into the Cr-rich oxides and hydroxides, which can facilitate the stability of the Cr-rich passive film in Cl-containing electrolyte. Mo has been confirmed to have analogous pitting resistance in HEAs [11,37–40]. FeCoCrNiMo$_x$ (x = 0, 0.1, 0.3, 0.6) exhibited an increase in E_{pit} with the addition of Mo in 3.5 wt.% aqueous NaCl as seen in Figure 4a, which demonstrated that the doping with Mo made the passive film more resistant to Cl$^-$ [41]. According to the XPS results (Figure 4b,c), it could be concluded that the addition of Mo facilitated the deprotonation of Cr(OH)$_3$, and hence more Cr$_2$O$_3$ were detected in the film [38–41]. Moreover, the existence of Mo-oxide mainly MoO$_4^{2-}$ in the film could defend against corrosion attack, which also accounted for the high pitting resistance. It was reported that the alloying of Mo reduced the charge carrier density of the film but elevated the i_{pass} in 0.5 M aqueous H$_2$SO$_4$ (Figure 4d,e) [38]. This was because an increase in Mo interstitial cations with a higher oxidation state could lead to a decrease in the other interstitial cations to maintain electric neutrality and lattice conservativeness, and thus resulted in an enhanced i_{pass}.
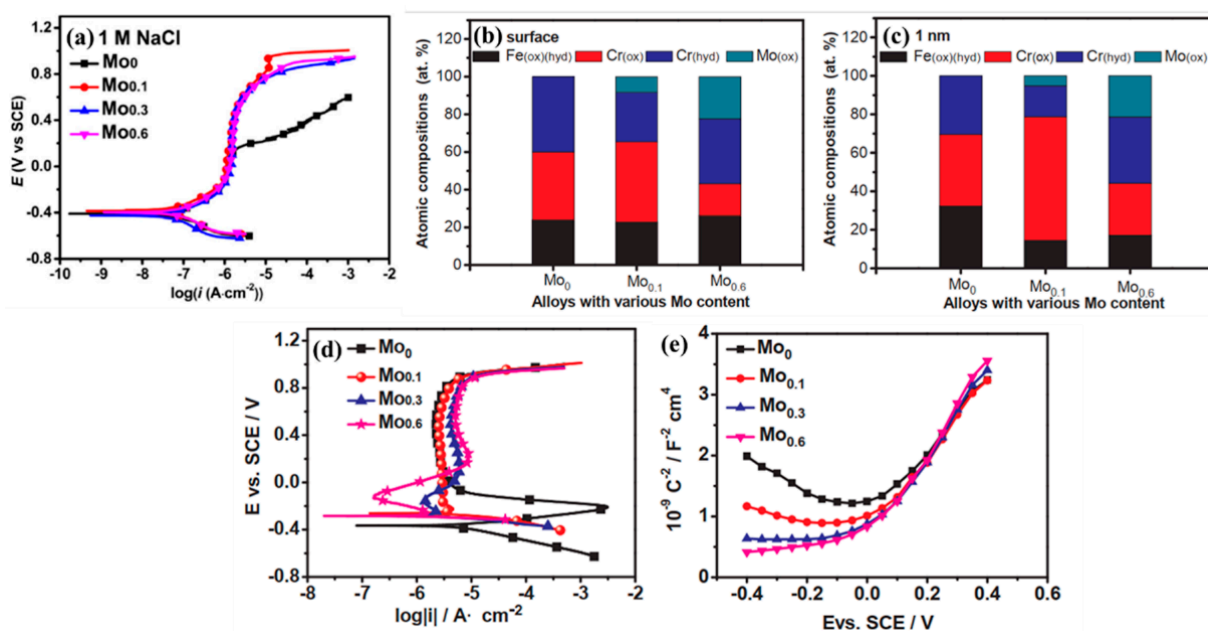

Figure 4. The polarization behavior and the surface chemistry for FeCoCrNiMo$_x$ (x = 0, 0.1, 0.3, 0.6) HEAs. (**a**) Potentiodynamic polarization plots of FeCoCrNiMo$_x$ in 1 M NaCl aqueous solution; the content percentages of Fe$_{(ox)(hyd)}$, Cr$_{(ox)}$, Cr$_{(hyd)}$ and Mo$_{(ox)}$ within the surface layers of Mo$_0$, Mo$_{0.1}$ and Mo$_{0.6}$ alloys: (**b**) the surface of the passive layers, and (**c**) the 1 nm depth of the passive layers; (**d**) potentiodynamic polarization curves and (**e**) Motto–Schottky plots after polarization for 4 h at 0.4 V$_{SCE}$ of FeCoCrNiMo$_x$ in 0.5 M H$_2$SO$_4$ [38,41].

2.4. Nickel

Nickel (Ni) is an important element to maintain FCC structure in stainless steel or HEA systems with high Cr content. Al$_2$CrFeCoCuTiNi$_x$ (x = 0, 0.5, 1.0, 1.5, 2.0) was proven to exhibit the lowest i_{corr} at x = 1.0 in NaOH and NaCl aqueous solutions [42]. The reason was that the lattice mismatch increased with the addition of Ni of small atomic radius. In H$_2$SO$_4$ aqueous solution, the increment of the Ni content deteriorated the corrosion resistance of the HEAs [43]. Ni preferred to be concentrated upon the surface of Co$_x$Cr$_2$Ni$_y$AlTi and tended to form a NiS layer that was unstable. This layer could accelerate the dissolution of

the passive film and induce the diffusion of S inside the alloy. With increasing Ni content, the content of NiS and S would increase, leading to a decline in corrosion resistance for the $CoCr_2Ni_3AlTi$ HEAs.

2.5. Aluminum

Aluminum (Al) is an appropriate choice for the high strength and light weight of HEAs. But compared with other elements, it ranks lower in the galvanic series, usually leading to preferential corrosion or dissolution. Generally, the addition of Al can generate an increment of i_{corr} and a reduction in E_{corr}, which shows that Al deteriorates the general corrosion resistance. Shi et al. designed single phase solution $Al_x(CoCrFeNi)_{1-x}$ HEA films by magnetron sputtering [25], and confirmed the above conclusion (Figure 5a–c). Moreover, at a higher Al content, the i_{pass} increased, the E_{pit} decreased, and the passive film thickened. As seen in Figure 5d,e, the content of Al within the passive film increased continually from 22.3% to 81.7%, while the content of Cr decreased from 37.3% to12.5%, and hence the integrity and protectiveness of the passive films decreased [44]. Meanwhile, the reduction in bound water in the passive films reflected another reason for the deterioration in the corrosion properties. In Cl^--containing aqueous H_2SO_4, Al tended to generate $[Al(SO_4)]^+$ and $[Al(OH)SO_4]$, which easily combined with Cl^- and dissolved. This process could induce the initiation of pitting [45]. Despite this, the size and number of pits observed (Figure 5f,g) were quite small because pitting was much weaker than galvanic corrosion induced by multi-phase [16].
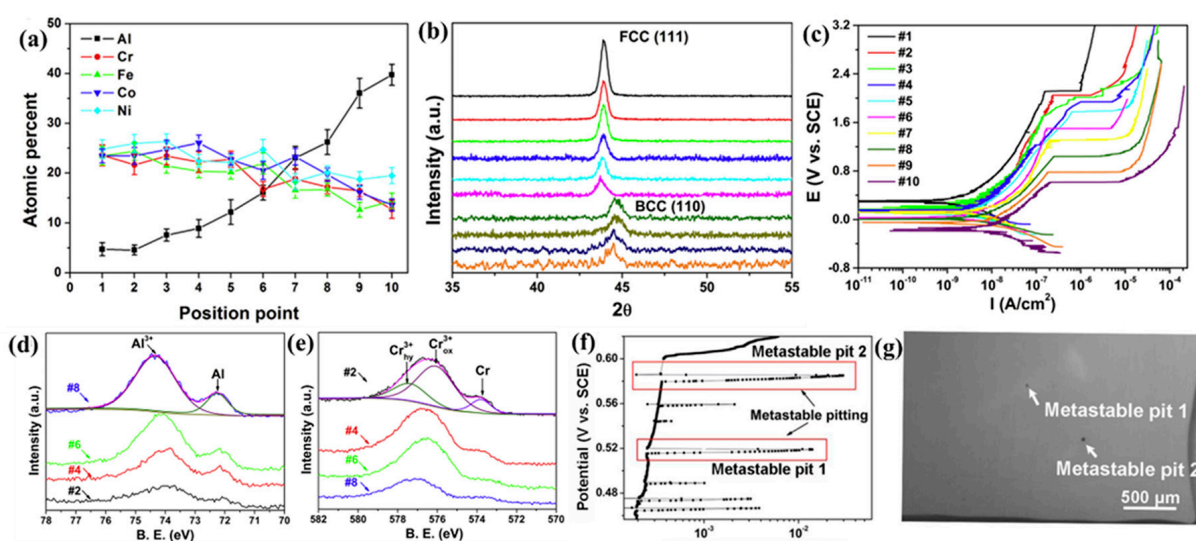

Figure 5. The polarization behaviors, surface chemistry, and pitting corrosion behaviors of $Al_x(CoCrFeNi)_{1-x}$ HEAs. (**a**) Chemical compositions vs. number of samples (spots 1 to 10); (**b**) XRD diffraction patterns of Al–containing HEA samples; (**c**) polarization plots of the ten HEA samples; #1–10 represent the $Al_x(CoCrFeNi)_{1-x}$ HEAs in (**a**); (**d**) Al 2p, (**e**) Cr 2p3/2 spectra of #2, #4, #6, and #8 HEA samples after immersion in 3.5 wt.% NaCl aqueous solution for 24 h; (**f**) enlarged current fluctuation of potentiodynamic polarization curves for $Al_{0.3}CoCrFeNi$, red boxes presents the enlarged current fluctuations; (**g**) corrosion micrograph after the polarization test at 0.6 V_{SCE} [25,46].

2.6. Manganese

The addition of manganese (Mn) to HEAs seems to be uniformly harmful to corrosion resistance aside from contributing to the stability of the FCC solution [47–50]. FeNiCoCrMn alloys showed an enhanced activation–passivation transition and a decrease in electrochemical impedance at low frequency from potentiodynamic polarization curves and electrochemical impedance spectroscopy (EIS) results [51]. This indicated that the addition of Mn retarded the process of passivation and reduced the stability of films for CoCrFeMnNi in aqueous H_2SO_4 solution. However, the i_{pass} was not affected because

the passive film compositions changed very little. Han et al. investigated the fate of Mn for NiFeCrMnCo by using atomic emission spectroelectrochemistry (AESEC) in 0.1 M NaCl solution [52]. Results demonstrated the passive films with Mn oxides had lower stability, and the negative effect of Mn on passivation was potential-sensitive. At lower passivation potential the dissolution of Mn occurred, together with minor amounts of Mn^{2+} incorporation in Cr-rich oxides. The considerable presence of Mn^{2+} in the Cr-rich oxides could be observed at higher potential. Moreover, Mn had a role of deteriorating the pitting corrosion resistance in Cl^--containing aqueous solution [53]. Mn can be considered for promoting the production of defects in the passive films and introducing the Mn-depleted oxide film from Cr compounds. This led to a poor pitting resistance of CoCrFeMnNi in a chloride solution compared to CoCrFeNi. Simultaneously, the pits grown at grain boundary paths were larger and deeper with the addition of Mn.

2.7. Other Metallic Elements

In addition to the common metallic elements discussed above, there are several other elements worth reviewing which have significant effects on corrosion behavior. This section briefly reviews the role of these metallic elements, including cobalt (Co), iron (Fe), niobium (Nb), tungsten (W), tin (Sn). It was reported that the appropriate addition of Co could obviously decrease the passivation current density for CoCrNiAlTi-based HEAs in H_2SO_4 aqueous solution [43] and the corrosion current density for AlNiYCox in 3.5 wt.% NaCl aqueous solution [54]. The electrochemical polarization and XPS results indicated that Co could effectively elevate the passive film stability and inhibit the hydrolysis of Cr^{3+} [43]. As for Fe element, the corrosion resistance of Fe-containing HEAs gradually deteriorated with the increase in the Fe content [55]. It was also indicated that pitting corrosion tended to initiate in Fe-rich HEAs. This was because Fe-based oxide and hydroxide could not have enough protective capacity. Nb, W, Sn are generally recognized as the pitting corrosion resistant elements. It was reported that the increasing content of Nb in CoCrFeNiMo contributed to a more stable passive film and a higher E_{pit} [56]. This was because, firstly, the Nb_2O_5 oxide could form upon the Nb-containing alloys, which exhibited low defect density and high pitting resistance. Secondly, Nb could improve the stability and compactness of Cr-oxide. Thirdly, Nb could inhibit the formation of Cr-rich $M_{23}C_6$ carbides and the resulting Cr-depleted zones. These three factors inhibited the initiation of pitting corrosion. The alloying of W or Sn in CoCrFeNi can possess obvious elevation of E_{pit}. It could be thus inferred that W or Sn addition increased the stability of the passive film by the formation of WO_3 or SnO_2 due to the negative oxide formation energy [57].

2.8. Non-Metallic Elements

The alloying of non-metallic elements can also affect the stability of passive film and pitting behavior of HEAs. Carbon (C) is generally utilized to elevate the strength and hardness of commercial steels and stabilize the austenitic phase. In CoCrFeMnNi, it was reported that the moderate addition of C could increase the E_{pit}, and decrease the number and size of pits [13]. The results indicated that C could improve the stability of passive film and the pitting resistance by increasing the enrichment of Cr and bound water within the film and decrease the point defect density.

In aqueous H_2SO_4, nitrogen (N) alloying of Cantor alloy greatly reduced the critical dissolution rate and current density required for passivation [58]. Driven by an oxygen reduction reaction, N-containing Cantor alloy had an enhanced ability of spontaneous passivation in acidic solution. It was found that the N alloying led to the decrease in the critical elemental current density required for passivation, inhibited the onset of active dissolution, and decreased the potential of primary passivation. The potentiodynamic polarization (Figure 6a) exhibited higher i_{pass} for N-containing Cantor alloy while the dissolution rates of the elements remained almost the same between the N-containing and N-free alloy, demonstrating a higher formation rate of insoluble oxide for N-containing Cantor alloy in the passive range. In the lower potential region (close to E_{corr}), Cantor alloy

was facilitated to dissolve but N-containing Cantor alloy was promoted to spontaneously passivate due to the existence of the dissolved oxygen. In Cl^--containing system, N alloying could increase E_{pit}, protection potential and the modulus of impedance, and simultaneously reduce pitting number and pit size, as observed in Figure 6b,c [33]. The passive film tended to be denser and thinner. The Cr content of passive film increased. N alloying inhibited acidification inside the iso-concentration layer by the following reaction:
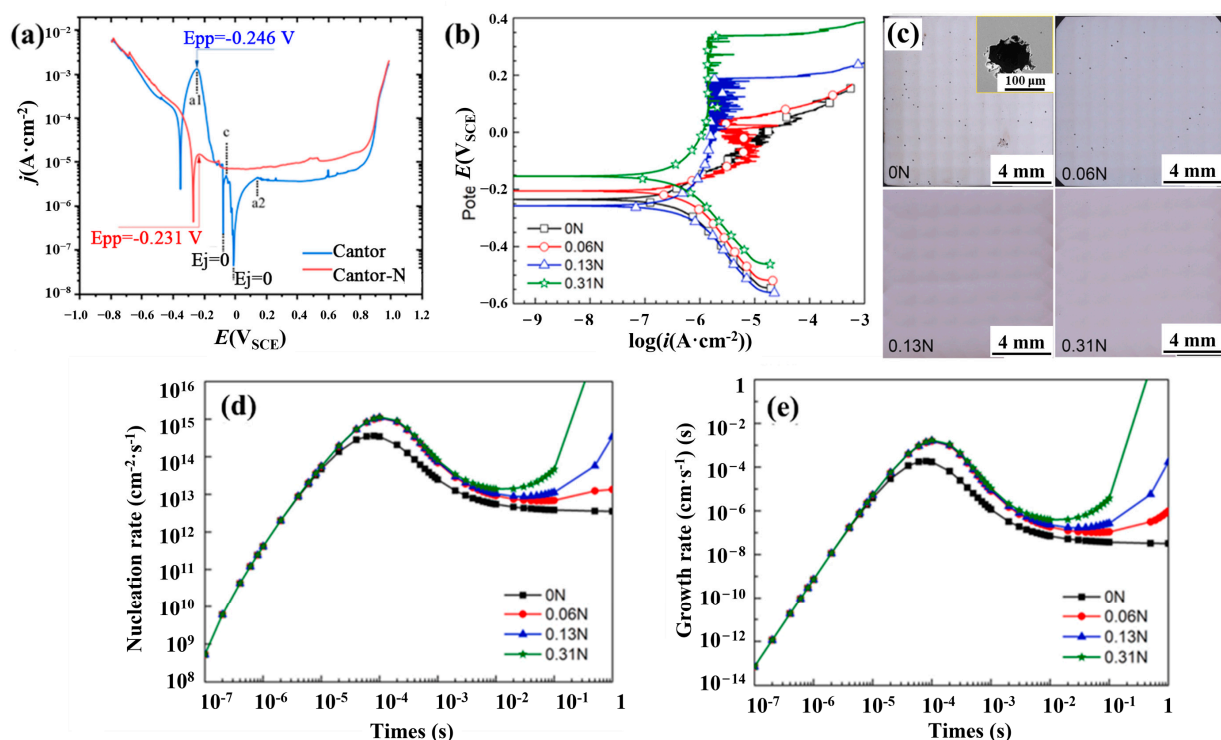
$$[N] + 3H^+ \rightarrow NH_3 \tag{1}$$

$$NH_3 + H_2O \leftrightharpoons NH_4^+ + OH^- \tag{2}$$

Figure 6. The effect of the addition of N on the polarization behaviors, pitting corrosion performance, and nucleation and growth processes of $CoCrFeMnNiN_x$. (**a**) The potentiodynamic polarization plots for CoCrFeMnNi and CoCrFeMnNiN in 0.1 M H_2SO_4 aqueous solution; (**b**) potentiodynamic polarization plots for CoCrFeMnNi and $CoCrFeMnNiN_x$ in 3.5 wt.% NaCl aqueous solution; (**c**) corrosion morphologies containing enlarged image (inset) after potentiostatic polarization; variation of nucleation rates of (**d**) Cr_2O_3 and (**e**) Fe_2O_3 within the passive films of $CoCrFeMnNiN_x$ [33,58].

With the dissolution progressing, the drop in pH value was obviously suppressed, and the degrees of the supersaturation for oxides and hydroxides was enhanced. The calculation verified the acceleration of the nucleation and growth for oxides and hydroxides such as Cr and Fe (Figure 6d,e). In the meantime, the consumption of H^+ could inhibit the self-catalytic pitting and improve the re-passivation ability.

Silicon (Si) is generally recognized as a non-passivated element, exhibiting impressive performance in HEAs. Choudhary et al. reported an AlFeMnSi HEA with low cost and low density, which exhibited spontaneous passivity and a wide passive range without the support of passive elements (Cr, Mo, Ti, W, Ta, Nb) [59]. Elemental dissolution analysis was conducted by using AESEC, which revealed cathodic dissolution of Si and subsequent precipitation of $Si(OH)_4$. Therefore, it formed a kind of protective passive film, which was composed of an inner Si/Al-rich oxide layer and an outer/precipitation Si-rich oxide/hydroxide layer. Based on this work, the author provided an idea for the composition design of corrosion resistant HEAs with no addition of conventional passive elements.

2.9. Design of High Corrosion Resistant HEAs

As mentioned above, HEAs have great freedom in composition and properties. Scully et al. [60] have emphasized the importance of the selection of alloying elements to improve the protectiveness of passive film and proposed some important points such as adding dopants that can improve the stability of the passive film or selecting elements that can form a new corrosion-resistant oxide. To date, tremendous amount of research has concentrated on HEAs that are equimolar or nearly equimolar. Nevertheless, the corrosion resistance of HEAs is not necessarily optimal with these compositions. In order to determine HEAs with superior corrosion resistance, it is significant to develop new approaches instead of only equimolar trial-and-error methods.

Integrated computational materials engineering (ICME) is a new method to develop materials with satisfactory properties through computational materials models with multi-scale analysis. Therefore, it is possible to design high corrosion resistance HEAs based on this new computational approach and corrosion theory. Through this idea, a new HEA, $Ni_{38}Cr_{21}Fe_{20}Ru_{13}Mo_6W_2$ alloy, was designed by Lu et al. [61]. In this system, Cr, Mo, and W could effectually improve corrosion properties as well as Ru could be useful to facilitate single FCC phase formation (Figure 7a). The E-pH diagram calculated by a modified version of CALPHAD, as shown in Figure 7b, indicated that this HEA could maintain a good passive state at a wide range of potentials and pH values. Indeed, this HEA exhibited excellent corrosion resistance, even in 6 M HCl solution [62]. Currently, the calculation of the E-pH diagram generally takes oxides or hydroxides as oxidation products. However, numerous research has indicated that non-stoichiometric oxides are prevalent in the passive film. To solve this problem, based on conventional E-pH diagrams, the non-stoichiometric oxides and the ions in aqueous solution for an FCC single-phase $Ni_{38}Fe_{20}Cr_{22}Mn_{10}Co_{10}$ HEA were conducted by Wang et al. [61], which presented a general and more accurate way to determine the reaction products during the corrosion process of HEAs.

Compared with conventional alloys, the composition of the passive film on HEAs is more complex. Thus, a comprehensive analysis of the species and contents of the film composition is of great significance for further designing corrosion resistant HEAs. Atom probe tomography (APT) is a modern method that can track elements and provide spatial locations for passive film. The compositional distributions of the passive film and the underlying alloy for $Ni_{38}Cr_{21}Fe_{20}Ru_{13}Mo_6W_2$ HEA after pre-passivation were determined through 3-D APT (Figure 7d–f) [63]. The film was Cr-rich and had the elements of Ni, Fe, Mo, and W in nonstoichiometric ratios, indicating the formation of a non-stoichiometric film. There existed an obvious peak of Mo composition adjacent to the alloy/film interface at about 0.5 nm, while W and Cr peak at about 2 nm, implying that the oxide began to separate into more stable, discrete stoichiometric phases. The film composition on the $Ni_{38}Fe_{20}Cr_{22}Mn_{10}Co_{10}$ HEA was also conducted by 3D-APT tests [62]. An unexpectedly high Cr enrichment within the passive film was observed, which might be attributed to a combination of kinetic and thermodynamic effects as well as depletion of other elements governed by chemical dissolution.

AESEC is a new technology in the corrosion field, especially the HEA corrosion field since it can directly and simultaneously analyze the dissolution rate of each element [63]. Therefore, this new method can be used to perform real time observations for the formation and dissolution of passive films on HEAs. Li et al. [63] studied evolution of the passive film on $Ni_{38}Cr_{21}Fe_{20}Ru_{13}Mo_6W_2$ HEA in H_2SO_4 solution, as shown in Figure 7g–j. In the cathodic activation process, the normalized Cr dissolution rate was faster than that of other elements, implying the dissolution of a Cr enriched oxide layer formed in air and/or water. In the potentiostatic passivation process, obvious enrichment of Cr and Ru occurred while the dissolution rates of W, Mo and Ni were approximately proportional to their bulk concentrations. The formation and dissolution of passive film on the $Ni_{38}Fe_{20}Cr_{22}Mn_{10}Co_{10}$ HEA were also recorded by AESEC and XPS [62]. The cation fraction of Cr in the film (but not found dissolved in solution) indicated that Cr enrichment occurred from the initial stage of the potentiostatic treatment.

Summarly, the emerging class of HEAs offers important opportunities to design new alloys with superior corrosion properties. Understanding the effect of major and minor alloying elements on corrosion resistance would enable rapid selection from the large base of principal elements. To achieve this, some new methods or experiments, such as ICME and AESEC, should be developed and used to clarify the intrinsic corrosion mechanism of HEAs.
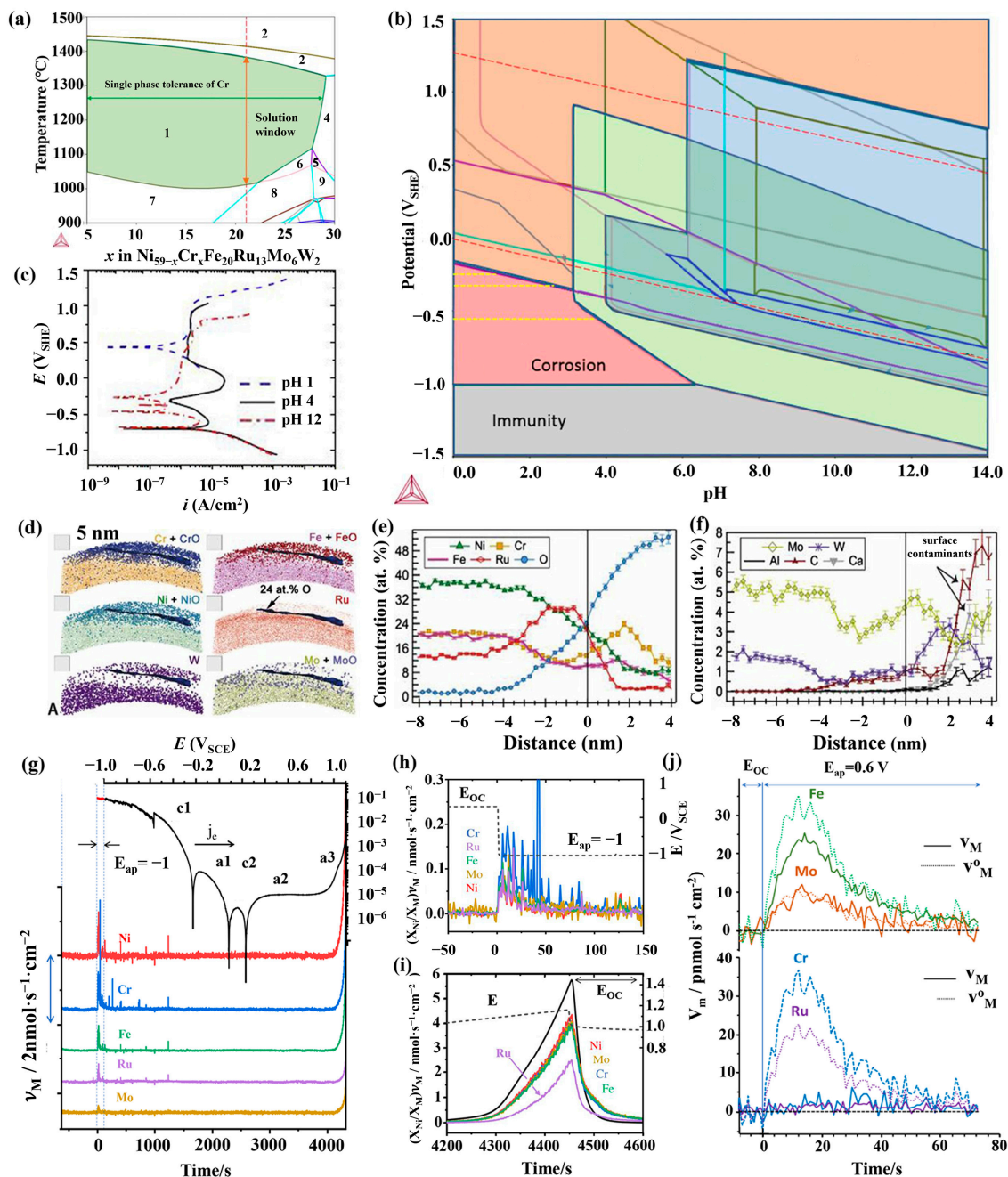

Figure 7. The design of corrosion resistant HEAs by using integrated computational materials engineering (ICME), and corresponding characterizations of the film chemistry and electrochemical behaviors. (**a**) Pseudo-binary phase diagram of the $Ni_{59-x}Cr_xFe_{20}Ru_{13}Mo_6W_2$ alloy system; (**b**) CALPHAD-calculated E-pH plots for $Ni_{38}Cr_{21}Fe_{20}Ru_{13}Mo_6W_2$ in 1 kg H_2O at 25 °C and 1 atm.; (**c**) potentiodynamic polarization curve of the $Ni_{38}Cr_{21}Fe_{20}Ru_{13}Mo_6W_2$ HEA in 0.1 M Na_2SO_4 solution with different pH; (**d–f**) APT characterization of the passive film formed on the HEA; (**g–i**) the polarization curve (upper) and the elemental dissolution rates (lower) of the HEA in de-aerated 2 M H_2SO_4; (**j**) elemental dissolution rates during a potentiostatic polarization at 0.6 V_{SCE} [63–65].

3. Influence of Structure on the Corrosion of HEAs

3.1. Single-Phase Solid Solution

Most of the HEAs take advantage of the high entropy effect to design single-phase solid solution and avoid the production of brittle intermetallic compound phases. Meanwhile, this contributes to a uniform and intact passive film. However, the high cooling rate during casting deviates from the equilibrium solidification, resulting in the growth of dendrites. Elements with low melting points (especially Cu) will separate into the interdendrites, and therefore galvanic corrosion will be generated. Homogenization or other methods can eliminate the element segregation between dendrites and interdendrites to form equiaxed crystals. In this case, the influence of grain size is worth considering. This section reviews the effect of element separation and the grain size for single-phase solid solution.

3.1.1. Dendritic Segregation

The solid solution generally crystallizes in a dendritic manner, and non-equilibrium solidification with a fast-cooling rate results in a difference in composition between the first crystallized dendrites and the later crystallized interdendrites. Cu with low melting point has been verified to be easily enriched in interdendrites [66]. It was reported that the presence of Cu in FeCoNiCrCu$_x$ alloys induced the change of failure mode from pitting corrosion to galvanic corrosion between the dendrites and interdendrites. The increase in Cu content enhanced the trend of localized corrosion. This was because a galvanic cell could be set up between Cu-rich interdendrites and Cr-rich dendrites, and the galvanic corrosion caused preferential dissolution along the interdentrites of Cu-containing HEAs [67]. The cross-sectional transmission electron microscope (TEM) image of CoCrFeNiCu corrosion features after immersion in 0.6 M NaCl aqueous solution showed the preferential corrosion of Cu-rich interdentrites, indicating the truth of galvanic corrosion [68]. The Cl$^-$ attacked the Cu-rich areas, resulting in the removal of Cu^{1+}. Galvanic corrosion stemmed from its different potential between the Cr-rich area (cathode) and the Cu-rich area (anode).

This Cu segregation-induced galvanic corrosion can be inhibited effectively. Yu et al. [69] reported a strategy of spark plasma sintering (SPS) to modify the formation of Cu from unwished segregation to homogeneous distribution for AlCoCrFeNiCu$_{0.5}$. The nanoscale Cu-rich phase uniformly precipitated in the grains. Compared with 304 stainless steels, the modified AlCoCrFeNiCu$_{0.5}$ displayed better corrosion resistance as well as higher strength and toughness. The plastic strain was increased by 1.65 times, R_{ct} was increased by 3.6 times, and i_{corr} was reduced by 11.2 times compared to the as-cast one.

Excessive addition of Cr could also cause its segregation. Both FeCoNi and FeCoNiCr$_{0.5}$ HEAs exhibited a fine columnar grain in the cross section and a cellular grain in the longitudinal section [32]. Nevertheless, in the FeCoNiCr alloy system, a further increment of Cr changed the microstructure from cellular to dendritic–interdendritic structure, and the Cr would be enriched at the dendritic arms. The inhomogeneity of the microstructure led to the obvious activation–passivation transition of the FeCoNiCr in 0.5 M H$_2$SO$_4$ electrolyte, and a lower E_{corr}, higher i_{corr} and i_{pass} in 3.5 wt.% NaCl aqueous solution than FeCoNi and FeCoNiCr$_{0.5}$. The deterioration of corrosion resistance was associated with the Cr segregation, since the nonuniform distribution of Cr resulted in the discrete growth of passive film. Simultaneously, the Cr-depleted area could be exposed to the solution, resulting in the galvanic dissolution at the interdendrites.

3.1.2. Grain Size

Grain refinement is generally utilized to obtain higher mechanical strength, while the resulting abundant grain boundaries may adversely affect corrosion resistance. Currently, there is limited attention on the effect of the grain size and grain boundary upon the corrosion resistance of HEAs. Wang et al. [70] investigated the influence of the grain size on the corrosion resistance of CoCrFeMnNi HEAs in 0.5 M H$_2$SO$_4$ aqueous solution. Potentiodynamic polarization results showed that the fine grain specimen (with an average grain size of 1.24 μm) and coarse grain specimen (with an average grain size of 145.9 μm)

all exhibited an activation–passivation region. This was because there existed the abundant grain boundaries in fine grain specimens. This could induce the galvanic corrosion between the inter-grains and the grain boundaries. The fewer channels of the coarse grain specimens might limit the element dissolution and diffusion. Correspondingly, it was less prone to form a stable and dense passive film. The XPS and nanoindentation tests indicated a more protective film of the medium grain specimen (with an average grain size of 71.6 μm), which was conductive to improve the corrosion resistance. Han et al. [71] studied the corrosion performance of ultra-fine grained (UFG) Cantor alloy in 3.5 wt.% NaCl aqueous solution. Results showed that the UFG alloy (with an average grain size of 0.689 μm) showed a lower pit corrosion resistance and an instability in the passive film, which was attributed to the high density of the grain boundary and the segregation of corrosion resistant elements.

3.2. Multi-Phase Solid Solution

Single-phase FCC or BCC HEAs have a single high toughness or high strength, but their incompatibility limits their development. Multi-phase HEAs balance the high strength and toughness and possess further application potential. However, the presence of a phase interface generally deteriorates corrosion resistance, and the potential difference between the two phases possibly induces severely galvanic corrosion.

The alloying of Al contributes to high strength for the generation of the Al-rich BCC phase. However, the adverse effects of this phase on corrosion resistance have been reported. Shi et al. [16,44,46] indicated that the BCC phase (rich in Al/Ni) gradually appeared in the FCC matrix (rich in Fe/Co/Cr) with the increase in Al content in $Al_x CrFeCoNi$ (x = 0.3, 0.5, 0.7), as depicted in Figure 8a. The E_b decreased distinctly and i_{pass} increased, demonstrating that the stability of passive film deteriorated with the increment of Al content, as shown in Figure 8b and Table 1. EIS results presented an accelerated rate of ions through the double-charge layer as indicated by the charge-transfer resistance. This reflected the relatively poor resistance to corrosion for high Al content HEAs. XPS implied that with the increase in Al content, the film became thicker with more Al oxide, which weakened the protective ability. The BCC phase was proven to be attacked by Cl^-, promoting the galvanic corrosion between two phases. There occurred the transition of the corrosion failure mode from pitting corrosion to selective corrosion of the BCC phase, as observed in Figure 8($c_1 - c_3$). Additionally, the higher the Al content (the lower the Cr content) in BCC, the easier the transition of metastable pitting corrosion to stable pitting became.

The aforementioned phase separation in multi-phase HEAs can be eliminated by homogenizing treatment and the galvanic corrosion is mitigated. Homogenization heat treatment effectively reduced the chemical segregation and improved corrosion resistance for AlxCoCrFeNi [17]. The heat treatment at 1250 °C for 1000 h caused a considerable variation of the microstructure. In $Al_{0.7}CoCrFeNi$, the dendritic structure transitioned into ~50 μm equiaxed grains (see Figure 9(a_1–a_3,b_1–b_3)). It was noted that, as shown in Figure 9(c_1,c_2), there occurred apparent compositional changes, particularly the Al, Cr, and Ni elements, across the interface of A2/B2 phases of the as-forged $Al_{0.7}CoCrFeNi$. Nevertheless, after the homogenizing process, there existed only a slight compositional gradient across the interface of A2/B2. From the polarization results (Figure 9(d_1,d_2)), $Al_x CoCrFeNi$ all exhibited a nobler E_{pit} and lower i_{pass} after homogenization heat treatment, indicating a better passive film stability and resistance to galvanic corrosion. This was ascribed to the reduction in the contact potential difference (V_{CPD}) or work function (WF) variations among phases (Figure 9(e_1,e_2)). The decreased tendency in WFs followed a sequence of A1 > A2 > B2. According to the corrosion morphology after polarization, the selective dissolution of $Al_{0.7}CoCrFeNi$ after homogenization heat treatment was significantly relieved (Figure 9(f_1,f_2)).
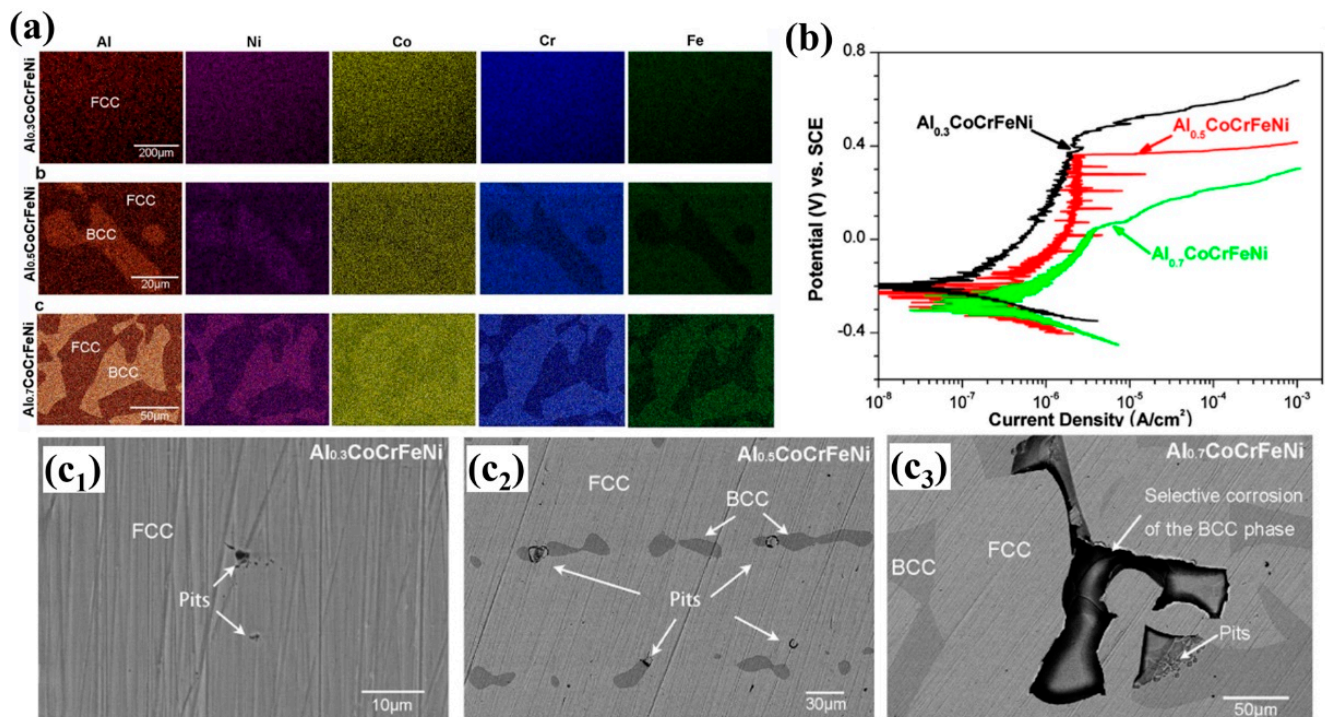
Figure 8. The microstructure, polarization behaviors, and corrosion failure morphologies of dual-phase $Al_xCoCrFeNi$ (x = 0.3, 0.5, and 0.7) HEAs. (**a**) The elemental distribution by EDS mappings in $Al_xCoCrFeNi$, in which the brown colour represents Al, the violet colour represents Ni, the yellow colour represents Ni, the blue colour represents Cr, and the green colour represents Fe; (**b**) potentiodynamic polarization curves in the 3.5 wt.% NaCl aqueous solution, in which the black curve is $Al_{0.3}CoCrFeNi$, the red curve is $Al_{0.5}CoCrFeNi$, the green curve is $Al_{0.7}CoCrFeNi$; and SEM micrographs after potentiodynamic polarization for the $Al_{0.3}CoCrFeNi$ (**c₁**), $Al_{0.5}CoCrFeNi$ (**c₂**) and $Al_{0.7}CoCrFeNi$ (**c₃**), the white arrows represent the corrosion pits and selective corrosion of BCC phase. [44].

Table 1. Electrochemical parameters of HEAs with various microstructure in the chloride-containing solution at room temperature.

Alloy	Microstructure	Solution	E_{corr} (mV)	i_{corr} (A/cm²)	E_{pit} (mV)	Ref.
As-forged $Al_{0.3}CoCrFeNi$	FCC	3.5 wt.% NaCl	−189	6.23×10^8	552	[17]
As-forged $Al_{0.5}CoCrFeNi$	FCC + BCC + B2	3.5 wt.% NaCl	−261	1.87×10^7	316	[17]
As-forged $Al_{0.7}CoCrFeNi$	FCC + BCC + B2	3.5 wt.% NaCl	−292	3.92×10^7	118	[17]
As-equilibrated $Al_{0.3}CoCrFeNi$	FCC	3.5 wt.% NaCl	−180	2.89×10^8	808	[17]
As-equilibrated $Al_{0.5}CoCrFeNi$	FCC + B2	3.5 wt.% NaCl	−228	7.14×10^8	496	[17]
As-equilibrated $Al_{0.7}CoCrFeNi$	FCC + BCC + B2	3.5 wt.% NaCl	−258	2.67×10^7	256	[17]
$Al_{0.5}CoCrFeNiTi_{0.5}$	FCC + BCC	3.5 wt.% NaCl	−320	5.32×10^7		[12]
$Al_{0.8}CoCrFeNiTi_{0.2}$	FCC + BCC	3.5 wt.% NaCl	−690	7.96×10^6		[12]
$Al_{1.0}CoCrFeNi$	BCC	3.5 wt.% NaCl	−270	5.61×10^7		[12]
As cast $AlCoCrFeNi_{2.1}$	Eutectic (FCC + B2) +precipitate (L12 + BCC)	3.5 wt.% NaCl	−423	1.42×10^6	298	[72]
Solution $AlCoCrFeNi_{2.1}$	Eutectic (FCC + B2)	3.5 wt.% NaCl	−422	1.48×10^6	255	[72]
Aging $AlCoCrFeNi_{2.1}$	Eutectic (FCC + B2) +precipitate (L12 + BCC)	3.5 wt.% NaCl	−428	1.94×10^6	361	[72]
$Al_{0.6}CrFeNi_{2.4}$	Eutectic (FCC + B2) +primary (FCC)	3.5 wt.% NaCl	−246	4.90×10^8	263.3	[73]
$Al_{0.8}CrFeNi_{2.2}$	Eutectic (FCC + B2)	3.5 wt.% NaCl	−256.6	2.44×10^7	199.2	[73]
$Al_{1.0}CrFeNi_{2.0}$	Eutectic (FCC + B2) +primary (B2)	3.5 wt.% NaCl	−296.2	4.59×10^7	165.8	[73]

Table 1. *Cont.*

Alloy	Microstructure	Solution	E_{corr} (mV)	i_{corr} (A/cm^2)	E_{pit} (mV)	Ref.
CoCrFeNiNb$_{0.15}$	Eutectic (FCC + Laves)	3.5 wt.% NaCl	−426	1.12×10^6	>1	[74]
CoCrFeNiNb$_{0.3}$	Eutectic (FCC + Laves)	3.5 wt.% NaCl	−409	7.10×10^7	>1	[74]
CoCrFeNiNb$_{0.45}$	Eutectic (FCC + Laves)	3.5 wt.% NaCl	−373	7.70×10^7	>1	[74]
FeCrNiCoNb$_{0.5}$ (L80)	eutectic (FCC + Laves) (L80)	3.5 wt.% NaCl	−173	2.29×10^8	993	[75]
FeCrNiCoNb$_{0.5}$ (L140)	Eutectic (FCC + Laves) (L140)	3.5 wt.% NaCl	−283	6.69×10^8	974	[75]
FeCrNiCoNb$_{0.5}$ (L250)	Eutectic (FCC + Laves) (L250)	3.5 wt.% NaCl	−299	1.46×10^7	958	[75]
FeCrNiCoNb$_{0.5}$ (L700)	Eutectic (FCC + Laves) (L700)	3.5 wt.% NaCl	−301	1.93×10^7	631	[75]
FeCrNiCoNb$_{0.5}$ (L1500)	Eutectic (FCC + Laves) (L1500)	3.5 wt.% NaCl	−310	2.17×10^7	411	[75]

The addition of Mo generally enhances the pitting resistance of the alloy, regardless of conventional alloy and HEAs. When Mo content was high, σ-CrMo tended to be precipitated as a strengthening phase, but it had the adverse effect on corrosion resistance. Dai et al. [38,41] analyzed the influence of the content of Mo on the microstructure and corrosion performance of FeCoCrNiMo$_x$. At lower Mo content, there occurred a transition from columnar grains (FeCoCrNi) to dendritic structure (FeCoCrNiMo$_{0.1}$) as seen in Figure 10(a$_1$,a$_2$). These two alloys presented severe surface spalling and pits (Figure 10 b$_1$,b$_2$ and c$_1$,c$_2$). With the increase in Mo content, the strip-shaped σ-CrMo phase clearly precipitated in the interdendrite region for FeCoCrNiMo$_{0.3}$ and FeCoCrNiMo$_{0.6}$ (Figure 10(a$_3$,a$_4$)). Scanning kelvin probe force microscopy (SKPFM) tests verified that the potential value of σ-CrMo was nobler than that of the nearby matrix (Figure 10d–f), and thus the matrix suffered from galvanic corrosion for the FeCoCrNiMo$_{0.3}$ and FeCoCrNiMo$_{0.6}$ (see Figure 10(b$_3$,b$_4$,c$_3$,c$_4$)).

Some non-metallic elements can also induce inferior corrosion properties, such as the precipitation of Cr-containing borides and carbides. Lee et al. [76] reported that with the increase in the B content the E_{corr} decreased and the i_{corr} increased for Al$_{0.5}$CoCrCuFeNiB$_x$ (x = 0, 0.2, 0.6 and 1.0). The deterioration of corrosion resistance was due to the depletion of Cr caused by the production of (Cr, Fe)B borides. The appearance of (Cr, Fe)$_{23}$C$_6$ could also reduce the content of Cr in the surrounding matrix, leading to the risk of pitting [13].

3.3. Eutectic High Entropy Alloys

Multi-phase HEAs can effectively accomplish the combination of the high strength and good ductility/toughness by a mixture of soft FCC and hard BCC phases. Nevertheless, the poor casting performance is always not ameliorated, which is a challenge especially at a large scale (kilogram scale). The emergence of eutectic high entropy alloys (EHEAs) seems to be a good solution direction. EHEAs exhibit bi-phase or tri-phase microstructure with mainly fine lamellar and a few rods, and thus are likely to present outstanding mechanical properties. Because of the isothermal process of the eutectic reaction, the casting defects such as shrinkage cavity and pore can be inhibited. However, the abundant phase interfaces provide conditions for local corrosion, which may limit its application in a corrosive environment.

An AlCoCrFeNi$_{2.1}$ alloy developed by Lu et al. [77–79] was the first EHEA system. This alloy consisted of FCC (rich in Fe/Co/Cr) and B2 (rich in Al/Ni) lamellar eutectic structure. Despite the good combination of hardness and fracture, AlCoCrFeNi$_{2.1}$ exhibited very similar i_{corr} with 304 stainless steel but a lower E_{pit} [80]. Selective dissolution of the B2 phase was proved to be the dominant mechanism of corrosion failure (see Figure 11(a$_1$–a$_5$)). This was because the loss of Cr in B2 promoted the generation of localized galvanic cells. The B2 phase with high tip potential was identified as anodic compared to the FCC matrix. The "area effect" of the B2 phase caused the accelerated corrosion. The FCC phase was

under protection during the corrosion process. Both FCC and B2 phases were covered by oxide scales after immersion, as seen in Figure 11(b_1–b_7). There appeared a dense film with a thickness of 20 nm upon the FCC phase, containing Fe, Cr, Ni, Co and O elements. As for B2 phase, the surface oxide scale was thicker and looser than the film on the FCC phase, mainly rich in Cr and O. HRTEM and the electron-diffraction patterns demonstrated that the two oxides had typical amorphous structures.
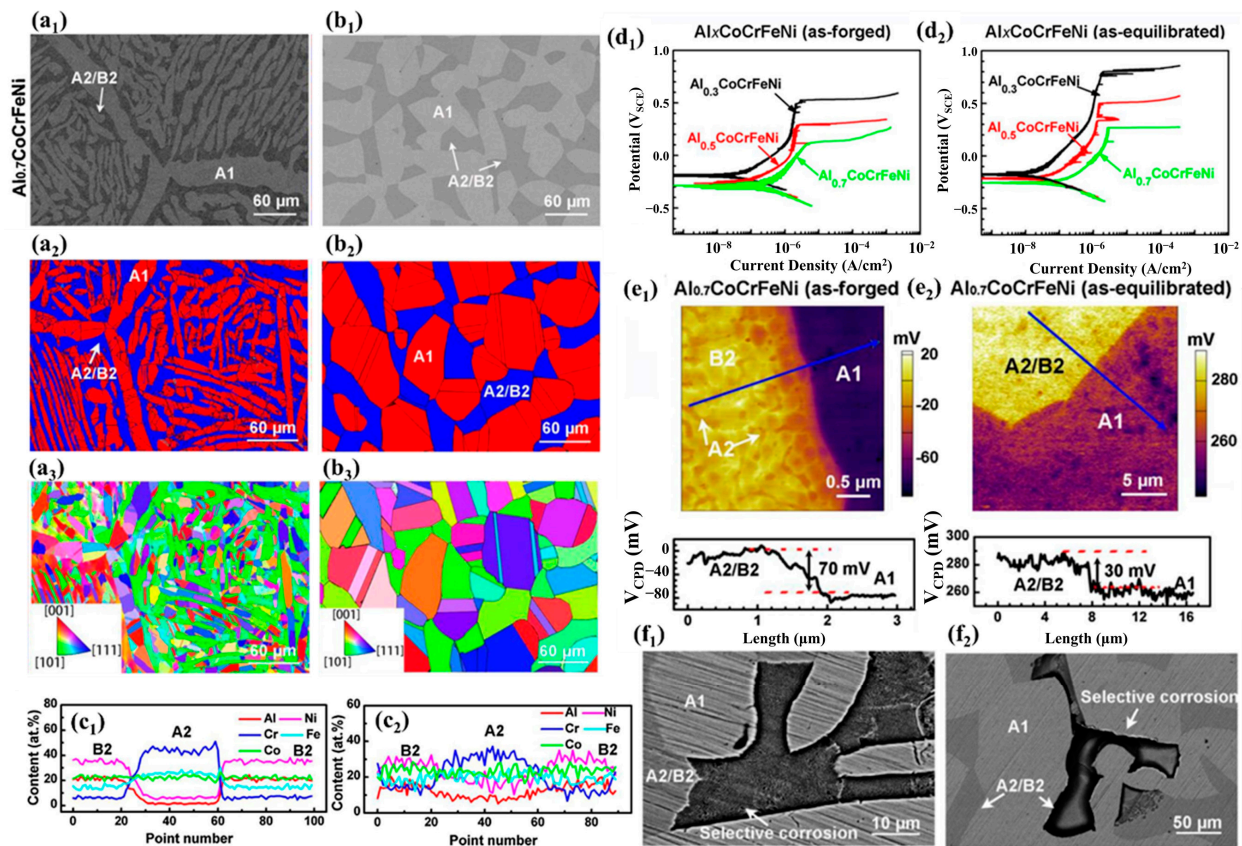

Figure 9. The effect of homogenization on the microstructure characterizations, electrochemical polarizations, and surface corroded morphologies for $Al_{0.7}CoCrFeNi$ HEAs. The surface morphology images, phase maps, and inverse pole-figures (IPF) of (a_1–a_3) the as-forged and (b_1–b_3) the as-equilibrated $Al_{0.7}CoCrFeNi$, the red areas are A1 phases while the blue areas are A2/B2 phases in (a_2,b_2), the different colours in (a_3,b_3) represent the grains with different oriented; the elemental distribution line-scanning by TEM-EDS of (c_1) the as-forged and (c_2) the as-equilibrated $Al_{0.7}CoCrFeNi$, the different colours of the lines represent different elements; potentiodynamic polarization plots of (d_1) the as-forged and (d_2) as-equilibrated $Al_{0.7}CoCrFeNi$ in 3.5 wt.% NaCl solution, in which the black curve is $Al_{0.3}CoCrFeNi$, the red curve is $Al_{0.5}CoCrFeNi$, the green curve is $Al_{0.7}CoCrFeNi$; (e_1) the contact potential difference (V_{CPD}) map and line scanning of the as-forged $Al_{0.7}CoCrFeNi$, the net-like A2 precipitates with a lower V_{CPD} distributed inside the bright B2 matrix; (e_2) V_{CPD} maps and line profiles for the as-equilibrated $Al_{0.7}CoCrFeNi$ at the phase boundary, the blue arrows are the line scanning sites, the bright areas are the phases with high V_{CPD}, and vice versa, the red dotted lines represent the average values of different phases; surface morphologies of (f_1) the as-forged and (f_2) the as-equilibrated $Al_{0.7}CoCrFeNi$ after the potentiodynamic polarization tests, the white arrows represent the selective corrosion of phases. [17].
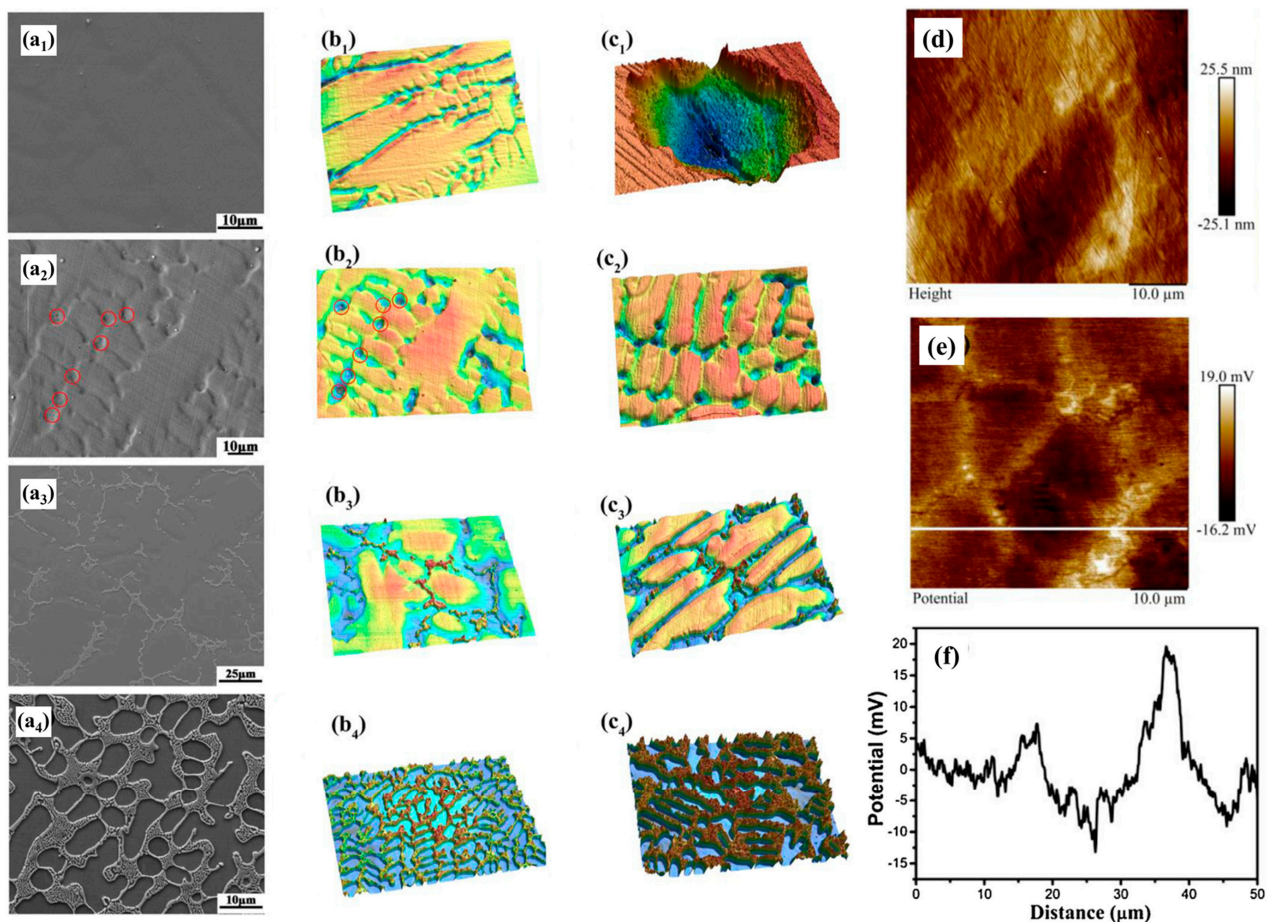
Figure 10. SEM morphologies and 3D characterizations of the FeCoCrNiMo$_x$ (x = 0, 0.1, 0.3, 0.6) alloy after the anodic polarization in 1 M NaCl aqueous solution: (**a$_1$–c$_1$**) FeCoCrNiMo$_0$ alloy, (**a$_2$–c$_2$**) FeCoCrNiMo$_{0.1}$ alloy in which the red circles are the regions of the anodic dissolution, (**a$_3$–c$_3$**) FeCoCrNiMo$_{0.3}$ alloy, and (**a$_4$–c$_4$**) FeCoCrNiMo$_{0.6}$ alloy. (**a$_1$–a$_4$**) and (**b$_1$–b$_4$**) SEM and 3D images after anodic polarization for 600 s; (**c$_1$–c$_4$**) 3D images after anodic polarization for 1800s; (**d**) topographical, (**e**) potential distribution mapping of the FeCoCrNiMo$_{0.3}$ alloy and (**f**) line-scanning results of the white line in (**e**) [41].

It was indicated that there occurred the island-like irregular regions and lamellar regular eutectic regions in AlCoCrFeNi$_{2.1}$ (Figure 11(c$_1$–c$_4$)) [27]. This special structure induced the formation of a new galvanic cell. The preferential corrosion of the B2 phase occurred in short-term corrosion, while the corrosion of the entire lamellar area took place dominantly in long-term corrosion as seen in Figure 11(d$_1$–d$_4$). As for Al$_x$CrFeNi$_{3-x}$ (x = 0.6, 0.8, 1.0) EHEAs, they showed similar corrosion behavior and failure mechanisms [73]. It was found that the B2 phase (rich in Al, Ni) possessed higher V_{CPD} and lower WF. This reflected that, more probably, the B2 phase was selectively dissolved in the NaCl aqueous solution. And such a dissolution corrosion was enhanced with the increment of Al in these alloys.

A number of works have been made to improve the corrosion performance of EHEA. Firstly, it was reported that the introduction of precipitation with nano-size could improve the corrosion resistance for EHEA. For example, a large number of L12 and BCC particles with a nano-size could precipitate in AlCoCrFeNi$_{2.1}$ after aging treatment [72]. This was beneficial to enhance the E_{pit}, and the corresponding electrochemical parameters are listed in Table 1. The average size of Al-rich L12 phase (~5 nm) inside FCC was too small to change the film upon the FCC phases, which maintained continuous and dense. The generation of Cr-rich BCC intermetallic inside the B2 phase enriched the Al content, and thus enhanced

the film stability. Secondly, substitution of Al with Nb has been verified to be a good choice to improve the corrosion properties of the alloy as seen in Table 1. As seen in Figure 12a–c, there appeared a typical lamellar eutectic structure with Laves (rich in Nb) and FCC (rich in Fe/Cr/Ni). It was noted that FeCoCrNiNb$_{0.5}$ exhibited unique integration of a lower i_{corr}, a nobler E_b and an enhanced re-passivation ability in 1 M NaCl aqueous solution, superior to most of traditional alloys and other HEAs [74,81]. Additionally, research showed that the corrosion properties of the EHEAs could be controlled by modifying the size of its lamellar eutectic structure [75]. A refined lamella microstructure in the EHEAs could lead to a more positive transpassivation potential as well as a lower i_{corr} compared with a coarsened lamella structure (Figure 12(d$_1$–d$_5$,e$_1$–e$_5$,f$_1$–f$_5$)). This was due to the formation of a more stable passive film to resist the absorption of Cl$^-$.
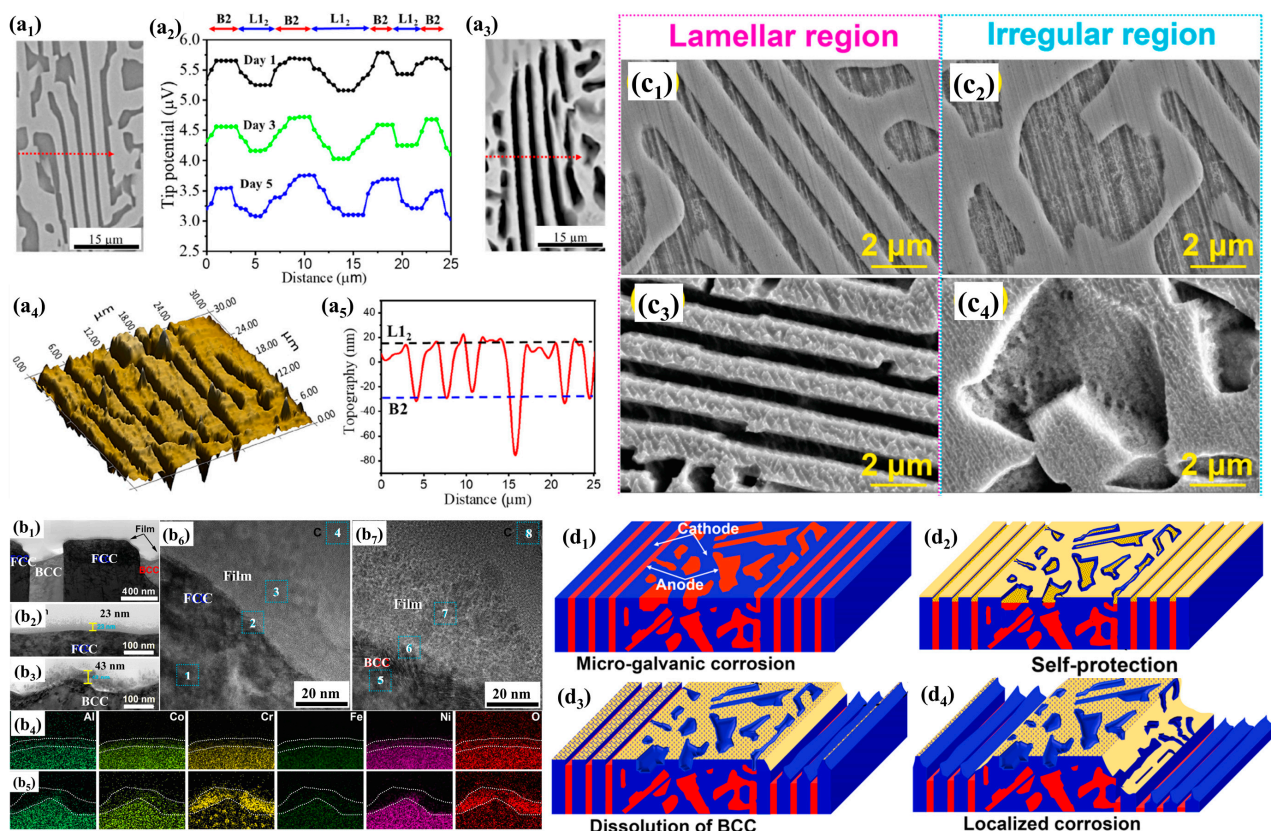

Figure 11. (**a$_1$**) SEM morphology of the eutectic AlCoCrFeNi$_{2.1}$ specimen surface; (**a$_2$**) line-scanning of eutectic AlCoCrFeNi$_{2.1}$ immersed in 1 wt.% NaCl aqueous solution at different time interval obtained at the dashed line; (**a$_3$**) corrosion morphology of the specimen after immersion for 5 days; 3D image (**a$_4$**) and line profile (**a$_5$**) of the corroded specimen showing preferential dissolution of B2 phase. TEM characterizations of corrosion product film upon specimen at 2 h: (**b$_1$**) BF-TEM morphology; (**b$_2$,b$_3$**) the magnified TEM images of films upon FCC and BCC phases; (**b$_4$,b$_5$**) elemental distribution of films upon FCC and BCC phases; (**b$_6$,b$_7$**) HRTEM images of film on FCC and BCC phase; (**c$_1$–c$_4$**) corrosion morphologies in different regions of EHEA in 0.5 M H$_2$SO$_4$ aqueous solution after being immersed for different times: 5 min and 8 h. The schematic of corrosion mechanism of EHEA: (**d$_1$**) micro-galvanic corrosion effect; (**d$_2$**) short-term self-protection; (**d$_3$**) the dissolution of surface BCC phase and the dissolution of FCC lamellas; (**d$_4$**) localized dissolution of lamellar region [27,80].
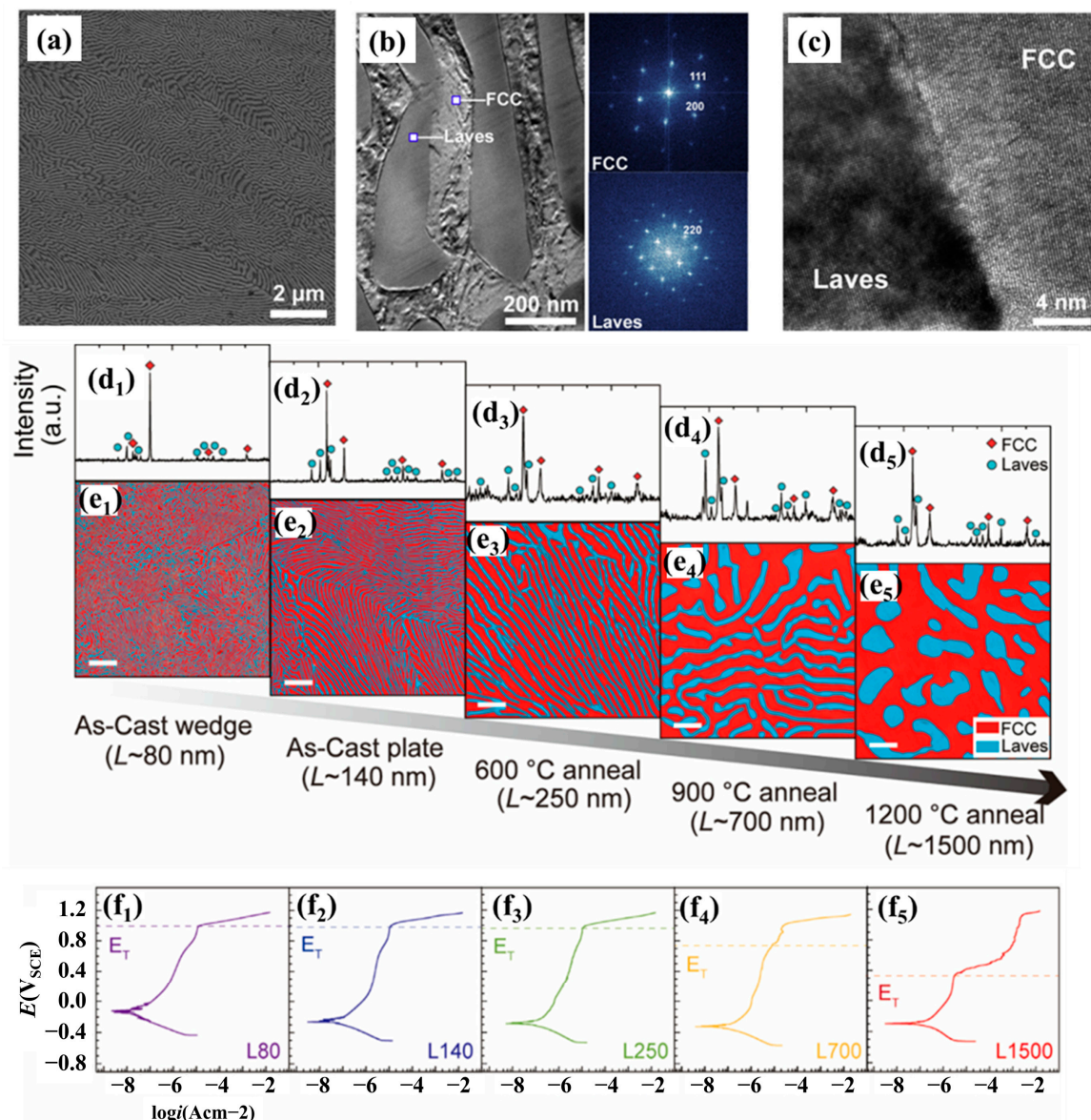
Figure 12. (**a**) the SEM morphology of the FeCrNiCoNb$_{0.5}$ EHEA; (**b**) the low magnification TEM morphology of FCC and Laves phases, and the corresponding FFT images in the inset; (**c**) the HRTEM image of the boundary of the phases; (**d$_1$**–**d$_5$**) XRD results and (**e$_1$**–**e$_5$**) the SEM images of the lamellar structure for the samples with different sizes of lamellar (note that scale bars are equal to 2 μm in (**e$_1$**–**e$_5$**)). (**f$_1$**–**f$_5$**) potentiodynamic polarization plots of samples with different sizes of lamellar [75,81].

4. Application for the Nuclear Industry

4.1. Lead–Bismuth Eutectic Environment

LBE alloy has great potential as coolant of nuclear reactors and nuclear waste disposal since it holds several advantages: high thermal conductivity of 14.2 W m^{-1} K^{-1} (723 K), high boiling point (1943 K) and low melting point (398 K). Therefore, LBE can provide an unrivalled efficiency, and avoid the risk of high temperature boiling and low temperature condensation. However, one of the crucial problems restricting its application is the capability of structural materials to resist the corrosion of high temperature liquid LBE [18,82,83].

The corrosion degradation of structural materials in liquid LBE environments is mainly divided into liquid metal embrittlement (LME) and liquid metal corrosion (LMC). Generally, LME could be initiated by the following mechanism [18]: the reduction in surface

energy and cohesion, dislocation emission, stress-assisted dissolution, atomic diffusion induced grain boundary penetration, and reinforced work hardening. LMC mainly includes dissolution and oxidation. Firstly, the metallic elements tend to dissolve directly in the LBE, which severely limits the service life of materials. Nb and Mo exhibit almost insoluble properties in LBE, while Ni, Mn, Ta, Co, Cr, and Fe have high solubility [83]. Secondly, oxidation is also a crucial problem during service. The presence of an appropriate level of dissolved oxygen, C_O, in LBE is necessary to ensure the protective oxide scales are formed. The oxide scales possibly protect matrix from dissolution. However, it can still form oxide inward without limit when the scales possess inadequate protection at a high Co level. "Active oxygen control" by controlling dissolved oxygen in LBE is an effective means of controlling corrosion rate [84,85]. But the high economic cost still drives the further development of structural materials to resist dissolution and oxygen corrosion.

In the past few decades, two kinds of commercial steels used in LBE environments, namely ferritic-martensitic steels (F/M steels) and austenitic stainless steels (AuSS) have received much attention. The tremendously investigated F/M steels [86] and AuSS [87,88] are the T91 (9Cr-1Mo grade) and the 316L, respectively. Other materials have also been developed, such as refractory alloys [89], oxide dispersion strengthened steels (ODS) [90–92], SiC_f/SiC composites [93], the MAX ($M_{n+1}AX_n$) phases [94,95], and HEAs [19,26,96]. Among these materials, HEAs exhibit good neutron swelling resistance, phase stability, and oxidation resistance, which possess great application potential.

Gong et al. reported the LME behavior for $Al_xCoCrFeNi$ HEAs in a liquid LBE environment. As for $Al_{0.7}CoCrFeNi$ HEA [96,97], it exhibited a dual-phase structure with a FCC phase (rich in Fe/Co/Cr) and a BCC phase (rich in Ni/Al). This alloy tended to be embrittled by LBE at 350 °C and 500 °C. The microstructure and embrittlement mechanism are depicted in Figure 13(a_1–a_3,b_1,b_2). At 350 °C, BCC phase was easily embrittled, resulting in the intragranular cracking. However, the main embrittlement mode transformed to the decohesion of the interface between the BCC and FCC phase at a temperature of 500 °C. Additionally, it was reported that there existed a BCC intergranular phase (rich in Ni/Al) containing a large number of Cr-rich nanosized particles in $Al_{0.4}CoCrFeNi$ HEA (Figure 13(c_1–c_3)) [19]. It exhibited a penetration exceeding an order of magnitude deeper than that of $Al_{0.3}CoCrFeNi$ with single-phase FCC structure (Figure 13(d_1,d_2)). This degraded corrosion property was associated with the energetic character of the boundaries of the BCC/FCC interphase and resultant wetting. Simultaneously, LBE could selectively leach Ni, which induced the transition from FCC to BCC. This would give rise to a serious LME problem.

Shi et al. investigated the oxidation behavior of $Al_xCrFeNi$ HEAs in an LBE environment. It displayed the protective bi-layer oxidation scale: $(Fe,Cr)_3O_4/Al_2O_3$ or $Cr_2O_3/(Al,Cr)_2O_3$ [24]. The $Cr_2O_3/(Al,Cr)_2O_3$ bi-layer tended to be thinner with increasing Al content. Further, it was noteworthy that the evolution of oxide scale in this alloy system was sensitive to the addition of elements [26]. With the addition of Cu, a thick oxide scale was identified in the form of a $Fe(Cr,Al)_2O_4$ outer layer and Al_2O_3 inner layer (Figure 14a). There existed a segregation of Cu between the oxide scale and alloy matrix, deteriorating the adherence of the oxide scale. The addition of Ti could facilitate the formation of TiO_2 and $TiAl_2O_5$ after 1000 h exposure. However, the oxide scale was changed as an outer layer of $PbTiO_3$, Cr_2O_3 and an inner layer of Al_2O_3 after a 2000 h exposure (Figure 14b), resulting in the degradation of the oxidation resistance. The addition of Nb exhibited beneficial effects on the oxidation resistance (Figure 14c). There appeared a thin oxide scale with Cr_2O_3 and Al_2O_3 after 1000 h exposure, and more Al_2O_3 tended to be formed in the oxide scale with the increase in exposure time.
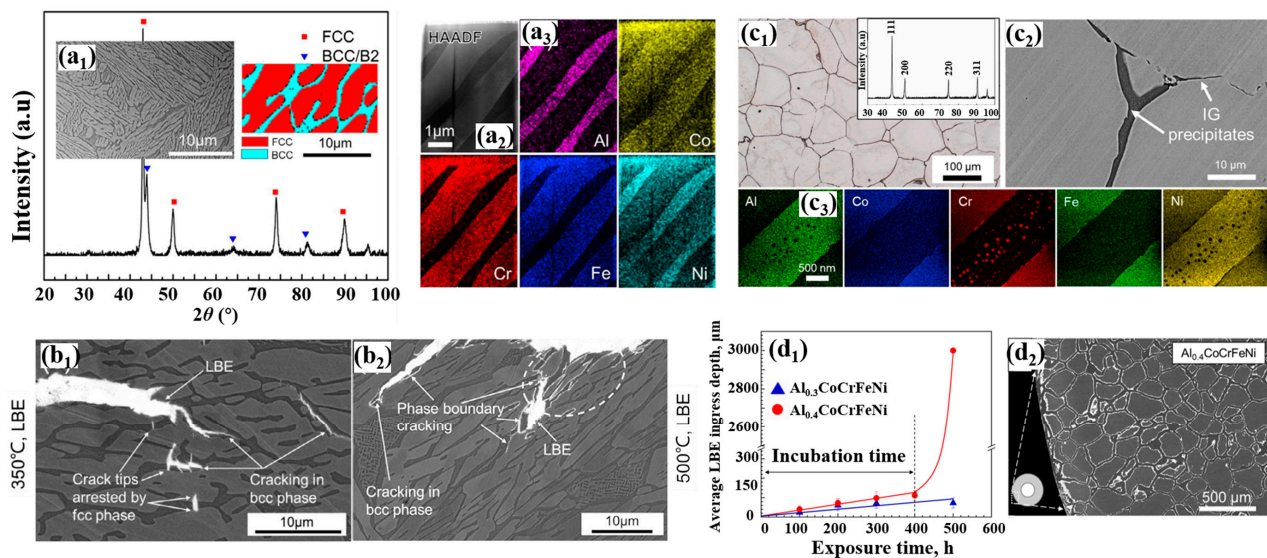
Figure 13. (**a₁**) SEM image, XRD pattern, and EBSD phase map; (**a₂**) HAADF morphology and (**a₃**) EDS elemental distribution of the dual-phase $Al_{0.7}CoCrFeNi$ HEA; SEM micrographs of the dual-phase $Al_{0.7}CoCrFeNi$ HEA after being immersed in LBE at (**b₁**) 350 °C and (**b₂**) 500 °C; (**c₁**) optical micrograph and XRD pattern of the $Al_{0.4}CoCrFeNi$ HEA; (**c₂**) BSE morphology of intergranular precipitates; (**c₃**) TEM-EDS maps of the intergranular precipitates; (**d₁**) the LBE ingress depth at grain boundaries of $Al_{0.3}CoCrFeNi$ and $Al_{0.4}CoCrFeNi$ HEAs; (**d₂**) BSE image of the $Al_{0.4}CoCrFeNi$ after being immersed in LBE at 500 °C for 500 h [19,96].

Figure 14. SEM and EDS line-scanning of the cross section of (**a**) AlCrFeNiCu, (**b**) AlCrFeNiTi and (**c**) AlCrFeNiNb after being immersed in 10^{-6} wt.% oxygen containing molten Pb at 600 °C for 1000 h, the red arrows represent the positions of the line-scanning, the blue arrow represent the transitional layer, the different colours of the lines represent different elements, and the dotted lines represent the boundary of the different layers [26].

Recently, the AlCrFeMoTi HEA coating with amorphous structure was prepared on F/M steel by magnetron sputtering [20]. This coating displayed high hardness, good interface adhesion, and phase stability at 500 °C. Compared with the F/M steel, it exhibited much better oxidation resistance with significantly thinner oxide scale as well as a lower weight loss of coating in LBE. The oxide scales were composed of Cr_2O_3, TiO_2 and $(Fe,Cr)_3O_4$. However, when the temperature reached 650 °C, there appeared elemental aggregation and oxidation in the coating, which enhanced the oxidation and failure of the coating. The addition of Si could further enhance the corrosion property [98]. A decrease in the coating weight loss could be obtained, which was due to the formation of more protective Cr_2O_3 and Al_2O_3 oxide scale. In addition, the effect of Au ions irradiation on the corrosion performance for coating was also investigated [99]. The Au-ions irradiation could lead to the crystallization of the AlCrFeMoTi amorphous HEA coating and created abundant grain boundaries, void defects, and dislocations. At low irradiation damage dose, the Au-ions' irradiation inhibited the weight loss and oxidation of coatings, which could be ascribed to the continuous and dense Cr-oxide scale. Nevertheless, at high irradiation damage dose, the elemental diffusion rate was accelerated, and the Cr-oxide layer became more porous, promoting the oxidation of the coating.

4.2. Supercritical Water Environment

When the temperature and pressure exceed 374 °C and 22.1 MPa, respectively, the chemical and physical behaviors of water, i.e., viscosity, density, and dielectric constant obviously change, namely SCW. SCW is a good solvent and reaction medium and has attracted much attention in many fields like nuclear reactors, catalysis and fossil fuel combustion plants. Nevertheless, the harsh operating conditions cause challenges to the structural materials utilized in SCW, due to the severity of oxidation caused by the high content of dissolved oxygen. The oxidation kinetics of alloys can be enhanced greatly in harsh environments. Therefore, preeminent performance of oxidation resistance is crucial for structural materials for service in such environments.

It has been reported that an $Al_{0.2}CoCrFeNi$ HEA thin film deposited by magnetron sputtering displayed a better corrosion resistance than G115 alloy [100]. It exhibited a bilayer structure in SCW: an outer layer composed of a large number of NiO and an inner layer composed of $NiFe_2O_4$ with a spinel structure. The dense and continuous inner spinel oxide scale could prevent the film from oxidation damage. Huang et al. reported the oxidation behavior of FeNiCrCuAl HEA in SCW [101,102]. The microstructure, oxidation kinetics, and surface oxidation scale are depicted in Figure 15. This alloy consisted of several different phases: a disordered BCC phase (rich in Fe/Cr) with numerous NiAl particles, a BCC phase (rich in Ni/Al), and an FCC phase (rich in Cu) (Figure 15a,b). Different oxide scales tended to be formed upon these phases in SCW. As for the disordered BCC phase (rich in Fe/Cr), it formed a porous outer $FeAl_2O_4$ oxide layer and a dense inner $FeCr_2O_4$ layer (Figure 15d). This bilayer oxide gradually turned into γ-Al_2O_3 and $CrAl_2O_4$ as the exposure period increased (Figure 15e). As for the BCC phase (rich in Ni/Al), there appeared a duplex structure oxide scale composed of an outer γ-Al_2O_3 layer and inner $NiAl_2O_4$ layer (Figure 15f). As for the FCC phase, many irregular Cu_2O particles precipitated upon the surface. This alloy exhibited significantly weakened oxidation kinetics than that of conventional alloys, indicating a better oxidation resistance.
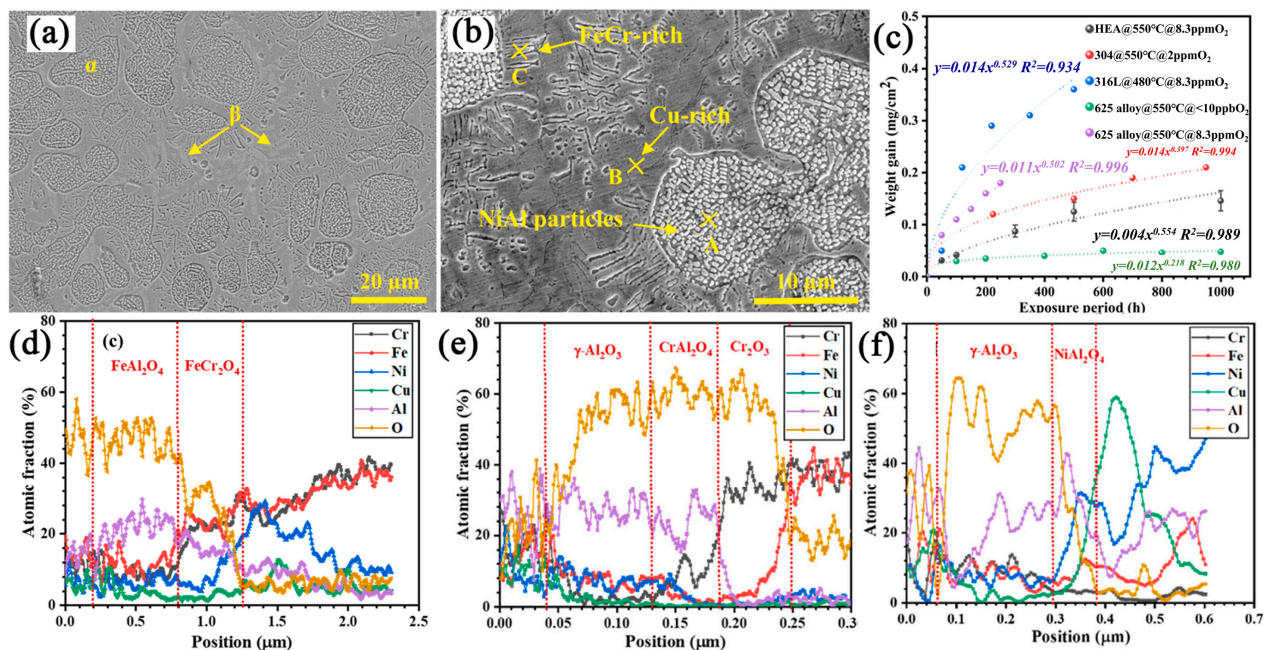
Figure 15. SEM morphologies of the FeNiCrCuAl HEA: (**a**) low magnification image, (**b**) high magnification image, and the yellow arrows show the phase distribution; (**c**) the weight gain curves vs. exposure period at 550 °C and 25 MPa in SCW for different materials; the line-scanning elemental distribution of the oxide films (**d**) upon the FeCr-rich BCC phase after being immersed at 550 °C and 25 MPa for 100 h, (**e**) upon the FeCr-rich BCC phase after being immersed at 550 °C and 25 MPa for 1000 h, and (**f**) upon the NiAl-rich phase after being immersed at 550 °C and 25 MPa for 100 h, the dotted lines represent the boundary of the different layers [101].

5. Conclusions

In this review, a general survey of corrosion performance and mechanisms in HEAs has been made. Especially, the effects of composition and structure of HEAs on their corrosion resistance, as well as from the perspective of the applications of some HEAs in special environments, have been summarized in detail.

It has been demonstrated that the corrosion behavior is very sensitive to the type of elements in HEAs. Cr and Ti are the most favorable passivation elements to ensure corrosion resistance. Mo is used as an auxiliary element to inhibit the initiation of pitting corrosion, which plays a role in stabilizing Cr oxide. Al and Mn are generally detrimental to corrosion resistance because they fail to form stable and dense films in aqueous solutions. N tends to enhance the ability of spontaneous passivation and accelerate the growth rate of insoluble oxide, which greatly improves the passive film stability. Dissolution of Si during cathodic polarization and deposition of $Si(OH)_4$ provide a stable film for HEAs. Combining corrosion theory and ICME, high corrosion resistant HEAs with a single phase can be successfully designed.

In the multi-phase HEAs, the galvanic corrosion or pitting corrosion can preferentially attack weak points, which will seriously deteriorate the corrosion resistance. Cu tends to form dendritic structures during the solidification, and interdendrites rich in Cu and poor in Cr suffer from serious corrosion. The increment of Al content is beneficial to facilitate the formation of the second phase rich in Al and Ni, but it is prone to lower the corrosion resistance. Cr and Mo can also lead to a degradative corrosion resistance through the formation of a Cr/Mo rich phase. Although EHEAs with specific microstructure exhibit higher application potential due to their good casting performance and excellent combination of toughness and strength, the problem of galvanic corrosion still needs to be further solved by alloying or microstructural modification.

Finally, the application of HEAs in LBE and SCW is summarized. The Al$_x$CoCrFeNi HEA tends to suffer from LME at 350 and 500 °C in LBE, because LBE selectively leaches Ni, which can induce the transition from FCC to BCC. The AlCrFeMoTi HEA coatings displays high hardness, good interface adhesion, phase stability, and outstanding oxidation resistance at 500 °C. The growth kinetics of the oxide films upon FeNiCrCuAl in SCW follows a parabolic law, indicating diffusion control of oxide growth. After being immersed in SCW, different scales on the surface of the alloy appear. This alloy presents good corrosion resistance in this harsh environment.

6. Future Work

This review aims to improve the understanding of the corrosion behavior and mechanism for HEAs. Therefore, based on the anti-corrosion performance improvement and practical application, some future works are suggested below (Figure 16).
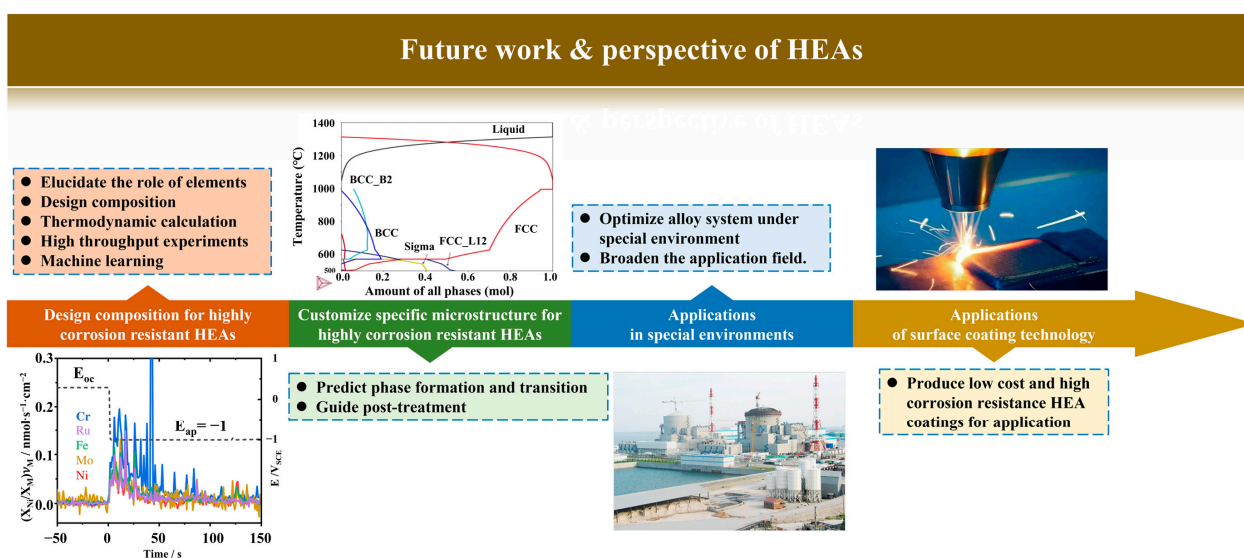

Figure 16. Proposed future work and perspectives for the corrosion fields of HEAs, including design composition for highly corrosion resistant HEAs, customized specific microstructures for highly corrosion resistant HEAs, applications in special environments, and applications of surface coating technology. The red part represents the composition design for highly corrosion resistant HEAs, the different colours of the lines represent different elements; the green part represents the customize specific microstructure for highly corrosion resistant HEAs, the blue part represents the application of HEAs in special environment, and the brown represents the application of HEAs of surface coating technology [26,63].

6.1. Composition Design for Highly Corrosion Resistant HEAs

The role of elements in corrosion properties in HEAs is still a problem that needs further elucidation, which could provide guidance for the design of highly corrosion resistant alloys. At present, although we understand their sluggish diffusion, lattice distortion and other characteristics, it is difficult to comprehensively find out the intrinsic difference of corrosion and passivation behavior between HEAs and traditional alloys. In situ monitoring of the dissolution process of elements by AESEC and analysis of the structure and composition of passive films by TEM and atomic force microscope (AFM) are helpful to understand the role of elements. Moreover, the compositional design of HEAs with high corrosion resistance by means of thermodynamic calculation, high throughput experiments, and machine learning is a key goal in the field of corrosion.

6.2. Tailoring Specific Microstructure for Highly Corrosion Resistant HEAs

The design and control of microstructures are essential since the homogenization of elemental distributions and microstructures could remarkably inhibit local corrosion. Therefore, it is necessary to predict phase formation and transition in terms of thermodynamic calculation, simulation, and machine learning. In addition, there is a lack of a certain guidance of thermo-mechanical treatment, which can enhance the corrosion properties through the attainment of homogeneous microstructures.

6.3. Applications in Special Environments

The unique structural characteristics of HEAs make them possible to be utilized in special harsh environments. As reviewed in this article, the neutron radiation resistance makes HEAs potential structural materials for nuclear power. Simultaneously, a great number of works are trying to use RHEAs instead of superalloys for temperatures above 1000 °C, due to their high temperature stability and oxidation resistance. It should be the focus of HEAs to optimize alloy systems in special environments and to broaden the application field.

6.4. Applications of Surface Coating Technology

The high cost of raw material and preparation makes the application of HEAs difficult. In surface protection, component repair, and other fields, the surface coating technology is one economical means of utilizing HEAs, such as laser cladding, electrodeposition, plasma-transferred arc cladding, thermal spraying, magnetron sputtering, and other techniques. HEA coatings or films may display superior corrosion performance than other coatings because of their relatively dense and uniform microstructural characteristics.

References

1. Yeh, J.-W.; Chen, S.K.; Lin, S.-J.; Gan, J.-Y.; Chin, T.-S.; Shun, T.-T.; Tsau, C.-H.; Chang, S.-Y. Nanostructured High-Entropy Alloys with Multiple Principal Elements: Novel Alloy Design Concepts and Outcomes. *Adv. Eng. Mater.* **2004**, *6*, 299–303. [CrossRef]
2. Yeh, J.-W.; Chang, S.-Y.; Hong, Y.-D.; Chen, S.-K.; Lin, S.-J. Anomalous decrease in X-ray diffraction intensities of Cu–Ni–Al–Co–Cr–Fe–Si alloy systems with multi-principal elements. *Mater. Chem. Phys.* **2007**, *103*, 41–46. [CrossRef]
3. Tsai, K.; Tsai, M.; Yeh, J. Sluggish diffusion in Co–Cr–Fe–Mn–Ni high-entropy alloys. *Acta Mater.* **2013**, *61*, 4887–4897. [CrossRef]
4. Wang, X.; Mercier, D.; Danard, Y.; Rieger, T.; Perrière, L.; Laurent-Brocq, M.; Guillot, I.; Maurice, V.; Marcus, P. Enhanced passivity of Cr-Fe-Co-Ni-Mo multi-component single-phase face-centred cubic alloys: Design, production and corrosion behaviour. *Corros. Sci.* **2022**, *200*, 110233. [CrossRef]
5. Senkov, O.N.; Miracle, D.B.; Chaput, K.J.; Couzinie, J.-P. Development and exploration of refractory high entropy alloys—A review. *J. Mater. Res.* **2018**, *33*, 3092–3128. [CrossRef]
6. Nagase, T.; Rack, P.; Noh, J.; Egami, T. In-situ TEM observation of structural changes in nano-crystalline CoCrCuFeNi multi-component high-entropy alloy (HEA) under fast electron irradiation by high voltage electron microscopy (HVEM). *Intermetallics* **2015**, *59*, 32–42. [CrossRef]

7.   Kumar, N.A.P.K.; Li, C.; Leonard, K.J.; Bei, H.; Zinkle, S.J. Microstructural stability and mechanical behavior of FeNiMnCr high entropy alloy under ion irradiation. *Acta Mater.* **2016**, *113*, 230–244. [CrossRef]

8.   Lu, Y.; Huang, H.; Gao, X.; Ren, C.; Gao, J.; Zhang, H.; Zheng, S.; Jin, Q.; Zhao, Y.; Lu, C.; et al. A promising new class of ir-radiation tolerant materials: Ti$_2$ZrHfV$_{0.5}$Mo$_{0.2}$ high-entropy alloy. *J. Mater. Sci. Technol.* **2019**, *35*, 369–373. [CrossRef]

9.   Zhao, Y.; Wang, M.; Cui, H.; Zhao, Y.; Song, X.; Zeng, Y.; Gao, X.; Lu, F.; Wang, C.; Song, Q. Effects of Ti-to-Al ratios on the phases, microstructures, mechanical properties, and corrosion resistance of Al$_{2-x}$CoCrFeNiTi$_x$ high-entropy alloys. *J. Alloys Compd.* **2019**, *805*, 585–596. [CrossRef]

10. Öztürk, S.; Alptekin, F.; Önal, S.; Sünbül, S.E.; Şahin, Ö.; İçin, K. Effect of titanium addition on the corrosion behavior of CoCuFeNiMn high entropy alloy. *J. Alloys Compd.* **2022**, *903*, 163867. [CrossRef]

11. Chou, Y.; Yeh, J.; Shih, H. The effect of molybdenum on the corrosion behaviour of the high-entropy alloys Co$_{1.5}$CrFeNi$_{1.5}$Ti$_{0.5}$Mo$_x$ in aqueous environments. *Corros. Sci.* **2010**, *52*, 2571–2581. [CrossRef]

12. Jiang, S.; Lin, Z.; Xu, H.; Sun, Y. Studies on the microstructure and properties of Al$_x$CoCrFeNiTi$_{1-x}$ high entropy alloys. *J. Alloys Compd.* **2018**, *741*, 826–833. [CrossRef]

13. Luo, H.; Zou, S.; Chen, Y.-H.; Li, Z.; Du, C.; Li, X. Influence of carbon on the corrosion behaviour of interstitial equiatomic CoCrFeMnNi high-entropy alloys in a chlorinated concrete solution. *Corros. Sci.* **2020**, *163*, 108287. [CrossRef]

14. Zhou, Q.; Sheikh, S.; Ou, P.; Chen, D.; Hu, Q.; Guo, S. Corrosion behavior of Hf$_{0.5}$Nb$_{0.5}$Ta$_{0.5}$Ti$_{1.5}$Zr refractory high-entropy in aqueous chloride solutions. *Electrochem. Commun.* **2019**, *98*, 63–68. [CrossRef]

15. Zhao, Y.; Qiao, J.; Ma, S.; Gao, M.; Yang, H.; Chen, M.; Zhang, Y. A hexagonal close-packed high-entropy alloy: The effect of entropy. *Mater. Des.* **2016**, *96*, 10–15. [CrossRef]

16. Shi, Y.; Collins, L.; Balke, N.; Liaw, P.; Yang, B. In-situ electrochemical-AFM study of localized corrosion of Al$_x$CoCrFeNi high-entropy alloys in chloride solution. *Appl. Surf. Sci.* **2018**, *439*, 533–544. [CrossRef]

17. Shi, Y.; Collins, L.; Feng, R.; Zhang, C.; Balke, N.; Liaw, P.; Yang, B. Homogenization of Al$_x$CoCrFeNi high-entropy alloys with improved corrosion resistance. *Corros. Sci.* **2018**, *133*, 120–131. [CrossRef]

18. Gong, X.; Short, M.P.; Auger, T.; Charalampopoulou, E.; Lambrinou, K. Environmental degradation of structural materials in liquid lead- and lead-bismuth eutectic-cooled reactors. *Prog. Mater. Sci.* **2022**, *126*, 100920. [CrossRef]

19. Gong, X.; Auger, T.; Zhu, W.; Lei, H.; Xiang, C.; Yu, Z.; Short, M.P.; Wang, P.; Yin, Y. Intergranular precipitation-enhanced wetting and phase transformation in an Al$_{0.4}$CoCrFeNi high-entropy alloy exposed to lead-bismuth eutectic. *Corros. Sci.* **2022**, *196*, 110038. [CrossRef]

20. Yang, J.; Shi, K.; Zhang, W.; Chen, Q.; Ning, Z.; Zhu, C.; Liao, J.; Yang, Y.; Liu, N.; Yang, J. A novel AlCrFeMoTi high-entropy alloy coating with a high corrosion-resistance in lead-bismuth eutectic alloy. *Corros. Sci.* **2021**, *187*, 109524. [CrossRef]

21. Pint, B.A. Performance of FeCrAl for accident-tolerant fuel cladding in high-temperature steam. *Corros. Rev.* **2017**, *35*, 167–175. [CrossRef]

22. Daghbouj, N.; Li, B.; Callisti, M.; Sen, H.S.; Karlik, M.; Polcar, T. Microstructural evolution of helium-irradiated 6H–SiC subjected to different irradiation conditions and annealing temperatures: A multiple characterization study. *Acta Mater.* **2019**, *181*, 160–172. [CrossRef]

23. Daghbouj, N.; Li, B.; Callisti, M.; Sen, H.; Lin, J.; Ou, X.; Karlik, M.; Polcar, T. The structural evolution of light-ion implanted 6H-SiC single crystal: Comparison of the effect of helium and hydrogen. *Acta Mater.* **2020**, *188*, 609–622. [CrossRef]

24. Shi, H.; Jianu, A.; Fetzer, R.; Szabó, D.V.; Schlabach, S.; Weisenburger, A.; Tang, C.; Heinzel, A.; Lang, F.; Müller, G. Compatibility and microstructure evolution of Al-Cr-Fe-Ni high entropy model alloys exposed to oxygen-containing molten lead. *Corros. Sci.* **2021**, *189*, 109593. [CrossRef]

25. Shi, Y.; Yang, B.; Rack, P.; Guo, S.; Liaw, P.; Zhao, Y. High-throughput synthesis and corrosion behavior of sputter-deposited nanocrystalline Al$_x$(CoCrFeNi)$_{100-x}$ combinatorial high-entropy alloys. *Mater. Des.* **2020**, *195*, 109018. [CrossRef]

26. Shi, H.; Fetzer, R.; Jianu, A.; Weisenburger, A.; Heinzel, A.; Lang, F.; Müller, G. Influence of alloying elements (Cu, Ti, Nb) on the microstructure and corrosion behaviour of AlCrFeNi-based high entropy alloys exposed to oxygen-containing molten Pb. *Corros. Sci.* **2021**, *190*, 109659. [CrossRef]

27. Wei, L.; Qin, W. Corrosion mechanism of eutectic high-entropy alloy induced by micro-galvanic corrosion in sulfuric acid solution. *Corros. Sci.* **2022**, *206*, 110525. [CrossRef]

28. Yan, X.; Guo, H.; Yang, W.; Pang, S.; Wang, Q.; Liu, Y.; Liaw, P.K.; Zhang, T. Al$_{0.3}$Cr$_x$FeCoNi high-entropy alloys with high corrosion resistance and good mechanical properties. *J. Alloys Compd.* **2020**, *860*, 158436. [CrossRef]

29. Yang, S.; Yu, W.; Liu, T.; Li, C.; Zhang, Y.; Qu, Y. Effect of Cr content on corrosion behavior of AlCr$_x$FeNi$_2$Cu$_{1.6}$ high entropy alloys. *Mater. Res. Express.* **2019**, *6*, 076501. [CrossRef]

30. Shimizu, H.; Yuasa, M.; Miyamoto, H.; Edalati, K. Corrosion Behavior of Ultrafine-Grained CoCrFeMnNi High-Entropy Alloys Fabricated by High-Pressure Torsion. *Materials* **2022**, *15*, 1007. [CrossRef]

31. Tsau, C.-H.; Tsai, M.-C.; Wang, W.-L. Microstructures of FeCoNiMo and CrFeCoNiMo Alloys, and the Corrosion Properties in 1 M Nitric Acid and 1 M Sodium Chloride Solutions. *Materials* **2022**, *15*, 888. [CrossRef]

32. Chai, W.; Lu, T.; Pan, Y. Corrosion behaviors of FeCoNiCr (x = 0, 0.5, 1.0) multi-principal element alloys: Role of Cr-induced segregation. *Intermetallics* **2020**, *116*, 106654. [CrossRef]

33. Feng, H.; Li, H.-B.; Dai, J.; Han, Y.; Qu, J.-D.; Jiang, Z.-H.; Zhao, Y.; Zhang, T. Why CoCrFeMnNi HEA could not passivate in chloride solution?—A novel strategy to significantly improve corrosion resistance of CoCrFeMnNi HEA by N-alloying. *Corros. Sci.* **2022**, *204*, 110396. [CrossRef]

34. Liu, J.; Liu, H.; Chen, P.; Hao, J. Microstructural characterization and corrosion behaviour of AlCoCrFeNiTi$_x$ high-entropy alloy coatings fabricated by laser cladding. *Surf. Coatings Technol.* **2019**, *361*, 63–74. [CrossRef]

35. Brox, B.; Yi-Hua, W.; Olefjord, I. Electrochemical and Surface Analyses of Mo (100) Single Crystal Polarized in 0.5 M H$_2$SO$_4$. *J. Electrochem. Soc.* **1988**, *135*, 2184–2187. [CrossRef]

36. Falkenberg, F.; Raja, V.; Ahlberg, E. An Alternative Explanation for the Apparent Passivation of Molybdenum in 1 mol/L Hy-drochloric Acid. *J. Electrochem. Soc.* **2001**, *148*, B132–B137. [CrossRef]

37. Shang, X.-L.; Wang, Z.-J.; Wu, Q.-F.; Wang, J.-C.; Li, J.-J.; Yu, J.-K. Effect of Mo Addition on Corrosion Behavior of High-Entropy Alloys CoCrFeNiMo$_x$ in Aqueous Environments. *Acta Met. Sin.* **2018**, *32*, 41–51. [CrossRef]

38. Dai, C.; Luo, H.; Li, J.; Du, C.; Liu, Z.; Yao, J. X-ray photoelectron spectroscopy and electrochemical investigation of the passive behavior of high-entropy FeCoCrNiMo$_x$ alloys in sulfuric acid. *Appl. Surf. Sci.* **2020**, *499*, 143903. [CrossRef]

39. Glowka, K.; Zubko, M.; Swiec, P.; Prusik, K.; Szklarska, M.; Chrobak, D.; Labar, J.; Stroz, D. Influence of Molybdenum on the Microstructure, Mechanical Properties and Corrosion Resistance of Ti$_{20}$Ta$_{20}$Nb$_{20}$(ZrHf)$_{20-x}$Mo$_x$ (Where: X=0, 5, 10, 15, 20) High Entropy Alloys. *Materials* **2022**, *15*, 393. [CrossRef]

40. Wang, J.; Chen, Y.; Zhang, Y.; Zhang, Y.; Li, J.; Liu, J.; Liu, Y.; Li, W. Microstructure evolution and acid corrosion behavior of CoCrFeNiCu$_{1-x}$Mo$_x$ high-entropy alloy coatings fabricated by coaxial direct laser deposition. *Corros. Sci.* **2022**, *198*, 110108. [CrossRef]

41. Dai, C.; Zhao, T.; Du, C.; Liu, Z.; Zhang, D. Effect of molybdenum content on the microstructure and corrosion behavior of FeCoCrNiMo$_x$ high-entropy alloys. *J. Mater. Sci. Technol.* **2020**, *46*, 64–73. [CrossRef]

42. Qiu, X.-W.; Liu, C.-G. Microstructure and properties of Al$_2$CrFeCoCuTiNi$_x$ high-entropy alloys prepared by laser cladding. *J. Alloys Compd.* **2013**, *553*, 216–220. [CrossRef]

43. Huang, L.; Wang, X.; Zhao, X.; Wang, C.; Yang, Y. Analysis on the key role in corrosion behavior of CoCrNiAlTi-based high entropy alloy. *Mater. Chem. Phys.* **2021**, *259*, 124007. [CrossRef]

44. Shi, Y.; Yang, B.; Xie, X.; Brechtl, J.; Dahmen, K.; Liaw, P. Corrosion of Al$_x$CoCrFeNi high-entropy alloys: Al-content and potential scan-rate dependent pitting behavior. *Corros. Sci.* **2017**, *119*, 33–45. [CrossRef]

45. Kao, Y.-F.; Lee, T.-D.; Chen, S.-K.; Chang, Y.-S. Electrochemical passive properties of Al$_x$CoCrFeNi (x = 0, 0.25, 0.50, 1.00) alloys in sulfuric acids. *Corros. Sci.* **2010**, *52*, 1026–1034. [CrossRef]

46. Shi, Y.; Mo, J.; Zhang, F.; Yang, B.; Liaw, P.; Zhao, Y. In-situ visualization of corrosion behavior of Al$_x$CoCrFeNi high-entropy alloys during electrochemical polarization. *J. Alloys Compd.* **2020**, *844*, 156014. [CrossRef]

47. Wong, S.-K.; Shun, T.-T.; Chang, C.-H.; Lee, C.-F. Microstructures and properties of Al$_{0.3}$CoCrFeNiMn$_x$ high-entropy alloys. *Mater. Chem. Phys.* **2018**, *210*, 146–151. [CrossRef]

48. Hsu, K.-M.; Chen, S.-H.; Lin, C.-S. Microstructure and corrosion behavior of FeCrNiCoMn$_x$ (x = 1.0, 0.6, 0.3, 0) high entropy alloys in 0.5 M H$_2$SO$_4$. *Corros. Sci.* **2021**, *190*, 109694. [CrossRef]

49. Sun, S.; Liu, H.; Hao, J.; Yang, H. Microstructural evolution and corrosion behavior of CoCrFeNiAl$_x$Mn$_{1-x}$ dual-phase high-entropy alloy coatings prepared by laser cladding. *J. Alloys Compd.* **2021**, *886*, 161251. [CrossRef]

50. Inman, S.; Han, J.; Gerard, A.; Qi, J.; Wischhusen, M.; Agnew, S.; Poon, S.; Ogle, K.; Scully, J. Effect of Mn Content on the Passivation and Corrosion of Al$_{0.3}$Cr$_{0.5}$Fe$_2$Mn$_x$Mo$_{0.15}$Ni$_{1.5}$Ti$_{0.3}$ Compositionally Complex Face-Centered Cubic Alloys. *Corrosion* **2022**, *78*, 32–48. [CrossRef]

51. Yang, J.; Wu, J.; Zhang, C.; Zhang, S.; Yang, B.; Emori, W.; Wang, J. Effects of Mn on the electrochemical corrosion and pas-sivation behavior of CoFeNiMnCr high-entropy alloy system in H$_2$SO$_4$ solution. *J. Alloys Compd.* **2020**, *819*, 152943. [CrossRef]

52. Han, J.; Li, X.; Gerard, A.; Lu, P.; Saal, J.; Frankel, G.; Ogle, K.; Scully, J. Potential Dependent Mn Oxidation and Its Role in Passivation of Ni$_{38}$Fe$_{20}$Cr$_{22}$Mn$_{10}$Co$_{10}$ Multi-Principal Element Alloy Using Multi-Element Resolved Atomic Emission Spectroelec-trochemistry. *J. Electrochem. Soc.* **2021**, *168*, 051508. [CrossRef]

53. Torbati-Sarraf, H.; Shabani, M.; Jablonski, P.D.; Pataky, G.J.; Poursaee, A. The influence of incorporation of Mn on the pitting corrosion performance of CrFeCoNi High Entropy Alloy at different temperatures. *Mater. Des.* **2019**, *184*, 108170. [CrossRef]

54. Zhang, S.; Zhang, Z.; He, P.; Hu, Z.; Jing, Z.; Gao, Y.; Liang, X. Role of Co content on the microstructure and anti-corrosion per-formance of high-hardness AlNiYCo$_x$ high entropy metallic glasses. *J. Non-Cryst. Solids* **2022**, *576*, 121268. [CrossRef]

55. Fan, Q.; Chen, C.; Fan, C.; Liu, Z.; Cai, X.; Lin, S.; Yang, C. Effect of high Fe content on the microstructure, mechanical and corrosion properties of AlCoCrFeNi high-entropy alloy coatings prepared by gas tungsten arc cladding. *Surf. Coat. Technol.* **2021**, *418*, 127242. [CrossRef]

56. Wen, X.; Cui, X.; Jin, G.; Liu, Y.; Zhang, Y.; Zhang, X.; Liu, E.; Tian, H.; Fang, Y. Corrosion and tribo-corrosion behaviors of nano-lamellar Ni$_{1.5}$CrCoFe$_{0.5}$Mo$_{0.1}$Nb$_x$ eutectic high-entropy alloy coatings: The role of dual-phase microstructure. *Corros. Sci.* **2022**, *201*, 110305. [CrossRef]

57. Niu, Z.; Xu, J.; Wang, T.; Wang, N.; Han, Z.; Wang, Y. Microstructure, mechanical properties and corrosion resistance of CoCrFeNiW$_x$ (x = 0, 0.2, 0.5) high entropy alloys. *Intermetallics* **2019**, *112*, 106550. [CrossRef]

58. Li, X.; Zhou, P.; Feng, H.; Jiang, Z.; Li, H.; Ogle, K. Spontaneous passivation of the CoCrFeMnNi high entropy alloy in sulfuric acid solution: The effects of alloyed nitrogen and dissolved oxygen. *Corros. Sci.* **2022**, *196*, 110016. [CrossRef]

59. Choudhary, S.; O'Brien, S.; Qiu, Y.; Thomas, S.; Gupta, R.; Birbilis, N. On the dynamic passivity and corrosion resistance of a low cost and low density multi-principal-element alloy produced via commodity metals. *Electrochem. Commun.* **2021**, *125*, 106989. [CrossRef]

60. Scully, J.R.; Inman, S.B.; Gerard, A.Y.; Taylor, C.D.; Windl, W.; Schreiber, D.K.; Lu, P.; Saal, J.E.; Frankel, G.S. Controlling the corrosion resistance of multi-principal element alloys. *Scr. Mater.* **2020**, *188*, 96–101. [CrossRef]

61. Wang, K.; Han, J.; Gerard, A.; Scully, J.; Zhou, B. Potential-pH diagrams considering complex oxide solution phases for understanding aqueous corrosion of multi-principal element alloys. *Npj Mater. Degrad.* **2020**, *4*, 11. [CrossRef]

62. Gerard, A.; Han, J.; McDonnell, S.; Ogle, K.; Kautz, E.; Schreiber, D.; Lu, P.; Saal, J.; Frankel, G.; Scully, J. Aqueous passivation of multi-principal element alloy $Ni_{38}Fe_{20}Cr_{22}Mn_{10}Ca_{10}$: Unexpected high Cr enrichment within the passive film. *Acta Mater.* **2020**, *198*, 121–133. [CrossRef]

63. Li, X.; Han, J.; Lu, P.; Saal, J.E.; Olson, G.B.; Frankel, G.S.; Scully, J.R.; Ogle, K. Communication—Dissolution and Passivation of a Ni-Cr-Fe-Ru-Mo-W High Entropy Alloy by Elementally Resolved Electrochemistry. *J. Electrochem. Soc.* **2020**, *167*, 061505. [CrossRef]

64. Lu, P.; Saal, J.E.; Olson, G.B.; Li, T.; Swanson, O.J.; Frankel, G.; Gerard, A.Y.; Quiambao, K.F.; Scully, J.R. Computational materials design of a corrosion resistant high entropy alloy for harsh environments. *Scr. Mater.* **2018**, *153*, 19–22. [CrossRef]

65. Quiambao, K.F.; McDonnell, S.J.; Schreiber, D.K.; Gerard, A.Y.; Freedy, K.M.; Lu, P.; Saal, J.E.; Frankel, G.S.; Scully, J.R. Passivation of a corrosion resistant high entropy alloy in non-oxidizing sulfate solutions. *Acta Mater.* **2018**, *164*, 362–376. [CrossRef]

66. Zhou, E.; Qiao, D.; Yang, Y.; Xu, D.; Lu, Y.; Wang, J.; Smith, J.A.; Li, H.; Zhao, H.; Liaw, P.K.; et al. A novel Cu-bearing high-entropy alloy with significant antibacterial behavior against corrosive marine biofilms. *J. Mater. Sci. Technol.* **2020**, *46*, 201–210. [CrossRef]

67. Hsu, Y.-J.; Chiang, W.-C.; Wu, J.-K. Corrosion behavior of $FeCoNiCrCu_x$ high-entropy alloys in 3.5% sodium chloride solution. *Mater. Chem. Phys.* **2005**, *92*, 112–117. [CrossRef]

68. Muangtong, P.; Rodchanarowan, A.; Chaysuwan, D.; Chanlek, N.; Goodall, R. The corrosion behaviour of $CoCrFeNi_x$ (x = Cu, Al, Sn) high entropy alloy systems in chloride solution. *Corros. Sci.* **2020**, *172*, 108740. [CrossRef]

69. Yu, Y.; Xu, N.; Zhu, S.; Qiao, Z.; Zhang, J.; Yang, J.; Liu, W. A novel Cu-doped high entropy alloy with excellent comprehensive performances for marine application. *J. Mater. Sci. Technol.* **2020**, *69*, 48–59. [CrossRef]

70. Wang, Y.; Jin, J.; Zhang, M.; Wang, X.; Gong, P.; Zhang, J.; Liu, J. Effect of the grain size on the corrosion behavior of CoCrFeMnNi HEAs in a 0.5 M H_2SO_4 solution. *J. Alloys Compd.* **2020**, *858*, 157712. [CrossRef]

71. Han, Z.; Ren, W.; Yang, J.; Tian, A.; Du, Y.; Liu, G.; Wei, R.; Zhang, G.; Chen, Y. The corrosion behavior of ultra-fine grained CoNi-FeCrMn high-entropy alloys. *J. Alloys Compd.* **2020**, *816*, 152583. [CrossRef]

72. Duan, X.; Han, T.; Guan, X.; Wang, Y.; Su, H.; Ming, K.; Wang, J.; Zheng, S. Cooperative effect of Cr and Al elements on passivation enhancement of eutectic high-entropy alloy $AlCoCrFeNi_{2.1}$ with precipitates. *J. Mater. Sci. Technol.* **2023**, *136*, 97–108. [CrossRef]

73. Zhao, Q.; Pan, Z.; Wang, X.; Luo, H.; Liu, Y.; Li, X. Corrosion and passive behavior of $Al_xCrFeNi_{3-x}$ (x = 0.6, 0.8, 1.0) eutectic high entropy alloys in chloride environment. *Corros. Sci.* **2022**, *208*, 110666. [CrossRef]

74. Zhang, M.; Zhang, L.; Liaw, P.; Li, G.; Liu, R. Effect of Nb content on thermal stability, mechanical and corrosion behaviors of hypoeutectic $CoCrFeNiNb_x$ high-entropy alloys. *J. Mater. Res.* **2018**, *33*, 3276–3286. [CrossRef]

75. Shuang, S.; Yu, Q.; Gao, X.; He, Q.; Zhang, J.; Shi, S.; Yang, Y. Tuning the microstructure for superb corrosion resistance in eutectic high entropy alloy. *J. Mater. Sci. Technol.* **2022**, *109*, 197–208. [CrossRef]

76. Lee, C.; Chen, Y.; Hsu, C.; Yeh, J.; Shih, H. The effect of boron on the corrosion resistance of the high entropy alloys $Al_{0.5}CoCrCuFeNiB_x$. *J. Electrochem. Soc.* **2007**, *154*, C424–C430. [CrossRef]

77. Lu, Y.; Dong, Y.; Jiang, H.; Wang, Z.; Cao, Z.; Guo, S.; Wang, T.; Li, T.; Liaw, P.K. Promising properties and future trend of eutectic high entropy alloys. *Scr. Mater.* **2020**, *187*, 202–209. [CrossRef]

78. Lu, Y.P.; Dong, Y.; Guo, S.; Jiang, L.; Kang, H.J.; Wang, T.M.; Wen, B.; Wang, Z.J.; Jie, J.C.; Cao, Z.Q.; et al. A Promising New Class of High-Temperature Alloys: Eutectic High-Entropy Alloys. *Sci. Rep.* **2014**, *4*, 6200. [CrossRef]

79. Lu, Y.; Gao, X.; Jiang, L.; Chen, Z.; Wang, T.; Jie, J.; Kang, H.; Zhang, Y.; Guo, S.; Ruan, H.; et al. Directly cast bulk eutectic and near-eutectic high entropy alloys with balanced strength and ductility in a wide temperature range. *Acta Mater.* **2017**, *124*, 143–150. [CrossRef]

80. Hasannaeimi, V.; Mukherjee, S. Galvanic corrosion in a eutectic high entropy alloy. *J. Electroanal. Chem.* **2019**, *848*, 113331. [CrossRef]

81. Shuang, S.; Ding, Z.; Chung, D.; Shi, S.; Yang, Y. Corrosion resistant nanostructured eutectic high entropy alloy. *Corros. Sci.* **2020**, *164*, 108315. [CrossRef]

82. Gong, X.; Li, R.; Sun, M.; Ren, Q.; Liu, T.; Short, M.P. Opportunities for the LWR ATF materials development program to contribute to the LBE-cooled ADS materials qualification program. *J. Nucl. Mater.* **2016**, *482*, 218–228. [CrossRef]

83. Zhang, J. A review of steel corrosion by liquid lead and lead–bismuth. *Corros. Sci.* **2009**, *51*, 1207–1227. [CrossRef]

84. Müller, G.; Schumacher, G.; Zimmermann, F. Investigation on oxygen controlled liquid lead corrosion of surface treated steels. *J. Nucl. Mater.* **2000**, *278*, 85–95. [CrossRef]

85. Tsisar, V.; Stergar, E.; Gavrilov, S.; Van Renterghem, W.; Louette, P.; Lucas, S. Effect of variation in oxygen concentration in static Pb-Bi eutectic on long-term corrosion performance of Al-alloyed austenitic steels at 500 degrees C. *Corros. Sci.* **2022**, *195*, 109963. [CrossRef]

86. Ye, Z.; Wang, P.; Dong, H.; Li, D.; Zhang, Y.; Li, Y. Oxidation mechanism of T91 steel in liquid lead-bismuth eutectic: With consideration of internal oxidation. *Sci. Rep.* **2016**, *6*, 35268. [CrossRef]

87. Chen, G.; Wang, J.; Zhang, H.; Li, L.; Fan, H. Low-temperature oxy-nitriding of 316 L austenitic stainless steel for improved corrosion resistance in liquid lead-bismuth eutectic. *Scr. Mater.* **2021**, *202*, 114014. [CrossRef]

88. Schroer, C.; Wedemeyer, O.; Novotny, J.; Skrypnik, A.; Konys, J. Selective leaching of nickel and chromium from Type 316 austenitic steel in oxygen-containing lead–bismuth eutectic (LBE). *Corros. Sci.* **2014**, *84*, 113–124. [CrossRef]

89. Cairang, W.; Ma, S.; Gong, X.; Zeng, Y.; Yang, H.; Xue, D.; Qin, Y.; Ding, X.; Sun, J. Oxidation mechanism of refractory Molybdenum exposed to oxygen-saturated lead-bismuth eutectic at 600 degrees C. *Corros. Sci.* **2021**, *179*, 109132. [CrossRef]

90. Ren, J.; Yu, L.; Liu, C.; Ma, Z.; Li, H.; Wang, Z.; Liu, Y.; Wang, H. Effects of Al addition on high temperature oxidation behavior of 16Cr ODS steel. *Corros. Sci.* **2022**, *195*, 110008. [CrossRef]

91. Xu, Z.; Song, L.; Zhao, Y.; Liu, S. The formation mechanism and effect of amorphous SiO_2 on the corrosion behaviour of Fe-Cr-Si ODS alloy in LBE at 550 degrees C. *Corros. Sci.* **2021**, *190*, 109634. [CrossRef]

92. Zhang, S.; Hayashi, S.; Ukai, S.; Oono, N. Effect of Co addition on the high-temperature oxidation behavior of ox-ide-dispersion-strengthened FeCrAl alloys. *Corros. Sci.* **2021**, *184*, 109391. [CrossRef]

93. Deck, C.; Jacobsen, G.; Sheeder, J.; Gutierrez, O.; Zhang, J.; Stone, J.; Khalifa, H.; Back, C. Characterization of SiC–SiC composites for accident tolerant fuel cladding. *J. Nucl. Mater.* **2015**, *466*, 667–681. [CrossRef]

94. Tunca, B.; Lapauw, T.; Callaert, C.; Hadermann, J.; Delville, R.; Caspi, E.N.; Dahlqvist, M.; Rosén, J.; Marshal, A.; Pradeep, K.G.; et al. Compatibility of Zr_2AlC MAX phase-based ceramics with oxygen-poor, static liquid lead–bismuth eutectic. *Corros. Sci.* **2020**, *171*, 108704. [CrossRef]

95. Wan, Q.; Wu, Z.; Liu, Y.; Yang, B.; Liu, H.; Ren, F.; Wang, P.; Xiao, Y.; Zhang, J.; Zhang, G. Lead-bismuth eutectic (LBE) corrosion mechanism of nano-amorphous composite TiSiN coatings synthesized by cathodic arc ion plating. *Corros. Sci.* **2021**, *183*, 109264. [CrossRef]

96. Gong, X.; Xiang, C.; Auger, T.; Chen, J.; Liang, X.; Yu, Z.; Short, M.P.; Song, M.; Yin, Y. Liquid metal embrittlement of a dual-phase $Al_{0.7}CoCrFeNi$ high-entropy alloy exposed to oxygen-saturated lead-bismuth eutectic. *Scr. Mater.* **2021**, *194*, 113652. [CrossRef]

97. Gong, X.; Chen, H.; Zhang, F.; Zhu, W.; Ma, H.; Pang, B.; Yin, Y. Degradation of tensile mechanical properties of two $Al_xCoCrFeNi$ (x = 0.3 and 0.4) high-entropy alloys exposed to liquid lead-bismuth eutectic at 350 and 500 °C. *J. Nucl. Mater.* **2022**, *558*, 153364. [CrossRef]

98. Yang, J.; Zhou, M.; Lv, L.; Zhou, Y.; Li, Q.; Liu, N.; Yang, J. Influence of Si addition on the microstructure, mechanical and lead-bismuth eutectic corrosion properties of an amorphous $AlCrFeMoTiSi_x$ high-entropy alloy coating. *Intermetallics* **2022**, *148*, 107649. [CrossRef]

99. Yang, J.; Zhang, F.; Chen, Q.; Zhang, W.; Zhu, C.; Deng, J.; Zhong, Y.; Liao, J.; Yang, Y.; Liu, N.; et al. Effect of Au-ions irradiation on mechanical and LBE corrosion properties of amorphous AlCrFeMoTi HEA coating: Enhanced or deteriorated? *Corros. Sci.* **2021**, *192*, 109862. [CrossRef]

100. Zhu, B.-H.; Qiu, H.-C.; Jiang, W.; Yu, Q.-H. Oxidation behavior of $Al_{0.2}CoCrFeNi$ high-entropy alloy film in supercritical water environment. *Rare Met.* **2022**, *41*, 1217–1222. [CrossRef]

101. Huang, X.; Zhan, Z.; Zhao, Q.; Liu, J.; Wei, L.; Li, X. Corrosion behavior of a dual-phase FeNiCrCuAl high entropy alloy in su-percritical water. *Corros. Sci.* **2022**, *208*, 110617. [CrossRef]

102. Zhan, Z.; Huang, X.; Zhao, Q.; Liu, J.; Wei, L.; Li, X. Effect of oxygen concentrations on the corrosion behavior of a duplex-phase FeNiCrCuAl high entropy alloy in supercritical water. *J. Nucl. Mater.* **2022**, *572*, 154046. [CrossRef]